

Master's Thesis

## **Màster Universitari en Enginyeria Industrial**

# **Numerical simulation of cavitation in a Francis runner**

**Thesis**

**Author:** Rafel Roig Bauzà  
**Supervisor:** Xavier Escaler Puigoriol  
**Call:** June 2017



Escola Tècnica Superior  
d'Enginyeria Industrial de Barcelona



## Abstract

Nowadays, two of the more important challenges for the humanity are the climate change and the management of the energy. For this reason the performance of a machine for the conversion of renewable energy has been studied in this thesis. Specifically, the GAMM Francis turbine runner working at its best efficiency point under cavitation conditions has been analysed using CFX (Ansys®).

Firstly, a slice of the 3D fluid domain has been made, using SolidWorks®, benefiting of the runner axisymmetry and thus decreasing the computational power needed. In order to take into account the runner rotation relative to the incoming flow field, three different domains have been defined. Two of the domains have been considered to be still and the other one has been considered to be in rotation around the turbine axis ensuring a model closer to the reality, which has permitted to study the relative and absolute velocity fields.

Then, a uniform incoming flow has been simulated through the runner blades under different levels of static pressure at the draft tube outlet boundary condition. The pressure has been gradually decreased, and consequently the sigma coefficient of cavitation, until the vapour pressure has been reached inside the runner. Thus, the onset of blade cavitation and its growth has been studied while keeping the remaining parameters unchanged.

Based on the numerical results, the value of the torque, the pressure coefficient and the shape, localization and size of the cavity have been analysed according to the sigma coefficient.

To finish a sensitivity study of the empirical parameters that the cavitation model takes into account has been carried out based on their impact on the cavitation results.



# Contents

<b>ABSTRACT</b>	<b>1</b>
<b>CONTENTS</b>	<b>3</b>
<b>1. NOMENCLATURE AND ABBREVIATIONS</b>	<b>5</b>
<b>2. PREFACE</b>	<b>7</b>
2.1. Origin of the thesis .....	7
2.2. Motivation .....	7
2.3. Previous requirements .....	7
<b>3. INTRODUCTION</b>	<b>8</b>
3.1. Objectives.....	8
3.2. Scope of the project .....	8
<b>4. BASIC CONCEPTS</b>	<b>9</b>
4.1. Fluid properties.....	9
4.2. Flow's equations.....	11
4.3. Boundary layer: Laminar and turbulent.....	13
4.4. Cavitation .....	14
4.5. Hydroelectric energy .....	16
4.6. Hill chart of an hydraulic turbine.....	21
4.7. Modelling the equations of flow.....	24
<b>5. CAVITATION IN TURBINES</b>	<b>27</b>
5.1. Cavitation numbers .....	27
5.2. Cavitation in Francis turbines.....	30
5.3. The Rayleigh Plesset Model .....	33
<b>6. COMPUTATIONAL MODEL</b>	<b>35</b>
6.1. The GAMM Francis turbine.....	35
6.2. Computational domain .....	36
6.3. Mesh.....	39
6.4. Turbulence model .....	44
6.5. Boundary conditions.....	45
<b>7. SIMULATIONS WITHOUT CAVITATION</b>	<b>51</b>
7.1. Monitored parameters.....	51

7.2. Analyse of the residues .....	52
7.3. Results of the simulations.....	53
<b>8. SIMULATIONS UNDER CAVITATION CONDITIONS _____</b>	<b>60</b>
8.1. Vapour volume fraction.....	60
8.2. Area covered by cavitation .....	63
8.3. Torque.....	65
8.4. Pressure coefficient .....	66
8.5. Head .....	75
8.6. Sensitivity analysis of the cavitation model .....	76
<b>9. ECONOMIC ANALYSIS _____</b>	<b>85</b>
<b>10. ENVIRONMENTAL IMPACT _____</b>	<b>86</b>
<b>11. WORK PLAN _____</b>	<b>87</b>
<b>CONCLUSIONS _____</b>	<b>89</b>
<b>ACKNOWLEDGEMENT _____</b>	<b>91</b>
<b>REFERENCES _____</b>	<b>92</b>

# 1. Nomenclature and abbreviations

A	Cross-section area [m <sup>2</sup> ]
C	Absolute velocity [m/s]
C <sub>p</sub>	Pressure coefficient [-]
C <sub>sound</sub>	Local speed of sound into the fluid [m/s]
C <sub>u</sub>	Projection of C on U direction [m/s]
D	Runner outlet diameter [m]
E	Specific energy [J/kg]
e <sub>rt</sub>	Loss coefficient [-]
g	Gravity [m/s <sup>2</sup> ]
H	Head [m]
h <sub>s</sub>	Setting level [m]
Ma	Mach number [-]
m <sub>fg</sub>	Shifted mass [Kg/s]
n <sub>s</sub>	Specific speed [rpm]
Q	Discharge [m <sup>3</sup> /s]
R	Radius [m]
R <sub>B</sub>	Bubbles radius [m]
Re	Reynolds [-]
U	Circumferential velocity [m/s]
V <sub>ref</sub>	Free stream velocity [m/s]
W	Relative velocity [m/s]

Z	Height [m]
$\alpha$	Vapour volume fraction [-]
$\rho$	Density [Kg/m <sup>3</sup> ]
$\psi$	Head coefficient [-]
$\mu$	Dynamic viscosity [kg/s·m]
$\nu$	Kinematic viscosity [m <sup>2</sup> /s]
$\gamma$	Specific weight of water [N/m <sup>3</sup> ]
$\eta$	Efficiency [-]
$\chi$	Local cavitation number [-]
$\sigma$	Sigma coefficient [-]
$\varphi$	Flow coefficient [-]
$\omega$	Runner angular velocity [rad/s]
$\Phi_i$	Volume fraction [-]
NPSE	Net positive suction specific energy
BEP	Best efficiency point
NVF	Nuclei volume fraction
SST	Shear Stress Transport
RANS	Reynolds Average Navier-Stokes

## 2. Preface

### 2.1. Origin of the thesis

The GAMM Francis turbine was designed for experimental research in the IMHEF hydraulic laboratory at Lausanne, Switzerland. It is one of the few turbines with public information available about its dimensions and the operation conditions, like efficiency, head, velocity and pressure distribution measurements.

For this reason, it was decided to carry out a computational model with CFX (Ansys®) benefiting from such detailed information in order to learn how to simulate cavitation in rotating runners of hydraulic turbines.

### 2.2. Motivation

One of the main branches of the Industrial Engineering degree is fluid mechanics, however only few courses are given at the ETSEIB (UPC).

On the other hand, the author has always admired all the machines used to generate power and believes that to improve energy system is a main challenge of the humanity.

For this reason, the author decided to simulate the working of the GAMM runner using CFX (Ansys®) under the supervision of Xavier Escaler.

### 2.3. Previous requirements

Knowledges about fluid dynamics and, specifically, about hydraulic machines and CFD are required to develop a model and to interpret correctly the results obtained from the simulations.

## 3. Introduction

### 3.1. Objectives

In this thesis project, the GAMM Francis turbine runner working at its best efficient point has been simulated numerically using the CFX (Ansys®) software without and with cavitation conditions. Firstly, the computational model without cavitation has been checked comparing the results obtained to the experimental ones. Then, the simulation of the cavitation on the blades has been carried out for various operation conditions.

Specifically, a multiphase flow simulation has been carried out considering a homogeneous mixture of water and vapour. The studies have been focused in the characteristics of the cavities as a function of the sigma number. The onset of cavitation has been forced decreasing the sigma number. On the other hand, a sensitivity study of some of the most important empiric parameters of the cavitation model (ZGB) has also been done.

The results obtained will be used to understand better the cavitation phenomenon, the simulation procedure and the influence of the cavitation on the turbine performance.

### 3.2. Scope of the project

The scope of the project is to achieve a reliable simulation of the flow across the GAMM Francis turbine runner, at its best efficiency point, under cavitation conditions.

Preliminary simulations will be made to understand the behaviour of the fluid when the turbine is working without cavitation. This solution will serve as an initial condition for the simulations with the cavitation module activated. For the cavitation simulations, the outlet pressure will be gradually decreased to reach the vapour pressure on the blade suction side while keeping the rest of parameters unchanged. Finally, a study of the impact on the results of some empirical parameters of the cavitation model will be carried out.

To conclude, the most important results will be analysed trying to understand the obtained results.

## 4. Basic concepts

Fluid mechanics is a branch of physics, especially of continuum mechanics since it studies models from a macroscopic viewpoint rather than from a microscopic one. Fluid mechanics is concerned with the mechanics of fluids and the forces of them, studying the interaction between the fluid and the solid bodies too. Usually numerical methods are required in order to be able to find the solution.

A brief view about the fluid mechanics' basic concepts will help us to understand the thesis work.

### 4.1. Fluid properties

#### 4.1.1. Viscosity

The viscosity of a fluid is a measure of its resistance to gradual deformation, which opposes the relative motion between the two surfaces of the fluid that are moving at different velocities, due to the forces of molecular cohesion.

The dynamic viscosity only appears in liquids which are in motion expressing its resistance to shearing flows when layers are moving parallel to each other with different speeds. It is defined like the relationship between shear stress and gradient of velocity [4].

On the other hand, kinematic viscosity is the division of the dynamic viscosity ( $\mu$ ) by the density of the fluid like it can be seen in equation 4.1. It is a basic concept when Reynolds number is analysed.

$$\nu = \frac{\mu}{\rho} \quad (\text{Eq. 4.1})$$

#### 4.1.2. Dimensionless numbers

##### 4.1.2.1. Volume fraction

The vapour volume fraction is a dimensionless parameter and one way of expressing the composition of a mixture. It is defined as the volume of a constituent  $V_i$  divided by the volume of all constituents of the mixture.

$$\phi_i = \frac{V_i}{\sum_j V_j} \quad (\text{Eq. 4.2})$$

#### 4.1.2.2. Mach number

The Mach number is a dimensionless parameter which is the ratio of flow velocity to the local speed of sound into the fluid. It is used to determine the flow compressibility or, what is the same, if the density changes over time and space [4].

$$Ma = \frac{V_{ref}}{c_{sound}} \quad (\text{Eq. 4.3})$$

#### 4.1.2.3. Reynolds number

The Reynolds number is an important dimensionless quantity used to help predict flow patterns in different fluid flow situations, mainly laminar versus turbulent. In particular, it is used to predict the transition from laminar to turbulent flow based on the characteristic length (L), viscosity ( $\nu$ ) and the free stream velocity of the fluid ( $V_{ref}$ ) [4].

$$Re = \frac{V_{ref} L}{\nu} \quad (\text{Eq. 4.4})$$

Low values of Reynolds indicate a laminar flow and high numbers of Reynolds indicates that the flow is turbulent. The transition Reynolds is stated at around 200000 for a typical external flow. For internal flows, it is between 2000 and 8000.

The laminar to turbulent transition Reynolds values also depend on [4]:

- The body surface temperature: generally, with low surface temperature the transition value is higher.
- The Mach number: with a higher value, the transition value is also higher.

#### 4.1.2.4. Pressure coefficient

The pressure coefficient, a dimensionless number, permits to describe the pressure evolution throughout a flow field in fluid dynamics [4]. It is widely used since its value is independent of the flow size and its value is constant if dynamic similarity is achieved between the experiment and in the full scale model [4]. It is defined here below:

$$C_p = \frac{P - P_{ref}}{\frac{1}{2} \rho V_{ref}^2} \quad (\text{Eq. 4.5})$$

Where  $P$  is the pressure in a given point,  $P_{ref}$  is the reference pressure,  $\rho$  is the density of water at 25°C and  $V_{ref}$  is the free stream velocity.

## 4.2. Flow's equations

### 4.2.1. Equations

#### 4.2.1.1. Continuity law

Fluid continuity is an expression of a more fundamental law of physics: the conservation of the mass. It tells that the mass flow rate is equals the product of average velocity times the cross-section area and times the fluid density must remain constant in a steady flow inside a control volume with solid boundaries and one inlet and one outlet [19].

$$\rho A V_{ref} = Kte \quad (\text{Eq. 4.6})$$

If the fluid is incompressible, then the volumetric flow rate is constant.

#### 4.2.1.2. Bernoulli's principle

Bernoulli's principle describes the behaviour of a fluid which is moving along a streamline. The simple form of Bernoulli's principle is valid for incompressible flows, whereby the viscosity can be omitted. It tells that in a steady flow, the sum of all form of energy in a fluid along a streamline is the same at all points on that streamline. This requires that the sum of kinetic energy, potential energy and static pressure remain constant [4].

$$\frac{C^2}{2} + \frac{P}{\rho} + gz = Kte \quad (\text{Eq. 4.7})$$

#### 4.2.1.3. Navier-Stokes equations

The Navier-Stokes equations, which are obtained applying the conservation laws in a differential volume of fluid, describe the motion of a viscous fluid substance. The solution of Navier-Stokes equations describes the velocity at each point of the flow over time. From the values of velocities, other quantities like pressure or temperature can be determined.

More specifically, the Navier-Stokes equations develop from the second law of Newton (conservation of the movement's continuity) and the conservation of the mass like it is shown in the next two equations [8]:

$$\rho \left( \frac{\partial u_i}{\partial t} + u \cdot \nabla u_i \right) = - \frac{\partial p}{\partial x_i} + \nu \Delta u_i + f_c^i \quad (\text{Eq. 4.8})$$

$$\frac{\partial \rho}{\partial t} + \nabla(\rho \cdot u) = 0 \quad (\text{Eq. 4.9})$$

### 4.2.2. Type of flows

There are different ways to categorize the flows based on their behaviour and the Mach number.

#### 4.2.2.1. Stationary and no stationary flow

- Stationary flow: the properties of the flow remain constants regardless of time.
- Non stationary flow: the properties of the flow do not remain constant over time.

#### 4.2.2.2. Compressible and incompressible flow

- Incompressible flow: the Mach number is lower than 0,3.
- Compressible flow: the Mach number is higher than 0,3.

#### 4.2.2.3. Subsonic and hypersonic flow

- Subsonic: the velocity of the flow is lower than the velocity of the sound in this fluid ( $Ma < 1$ ).
- Transonic: the velocity of the flow is similar to the velocity of the sound in this fluid ( $Ma = 1$ ).
- Supersonic: when the Mach number is higher than 1 and lower than 6.
- Hypersonic: when the velocity of the fluid is far larger than the velocity of the sound and Mach number is higher than 6.

## 4.3. Boundary layer: Laminar and turbulent

The region of the fluid in contact with a solid boundary where the fluid's behaviour is disturbed by the solid and the effects of the viscosity are dominant is called the Boundary Layer and a positive velocity gradient is found between fluid layers in contact.

The relative speed of the fluid particles inside the boundary layer increases from 0 m/s at the contact position to 99 per cent of the free stream velocity where the effects of the viscosity can be considered negligible [4].

Two different types of boundary layers can be defined according to their structure and the circumstances under which are created [4]:

- Laminar boundary layer: the laminar boundary layer is smoother than the turbulent since the turbulent contains swirls. The laminar flow creates less skin friction drag than the turbulent one, but it is less stable. The thickness of the boundary layer increases along the surface.
- Turbulent boundary layer: at some distance from the leading edge where the laminar boundary layer appears, the smooth laminar flow breaks down and a transition to a turbulent flow is observed. Then, the turbulent boundary layer starts to develop. The laminar flow tends to break down more suddenly than the turbulent layer.

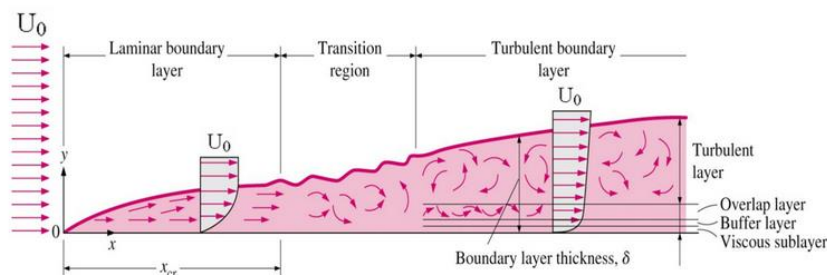


Figure 4.1: Boundary layer's structure [16]

## 4.4. Cavitation

Cavitation is a physical phenomenon which is characterized by the formation of bubbles in a liquid without external heating and due to a pressure drop under the vapour pressure. The cavities appear mainly at the carried nuclei by the liquid flow or micro particles because a pure substance can withstand much lower pressure than the vapour pressure without vaporization [18].

### 4.4.1. The cavitation process

The cavitation process can be divided in three phases [3]:

- Apparition: the formation of incipient bubbles from nuclei or micro particles, which are contained in the water and filled with air (or others gases) and vapour.
- Growth: the growth of the micro bubbles, which is a function of the initial radio of the nuclei and the external pressure. The growth is slow until a critical radio and then it becomes faster.
- Collapse: when the pressure increase again above the vapour pressure and the cavities condense quickly and a collapse is provoked inducing high pressure waves.

Although the first collapse is extremely fast, there are subsequent bounces due to the presence of remaining undissolved gas in the surrounding region.

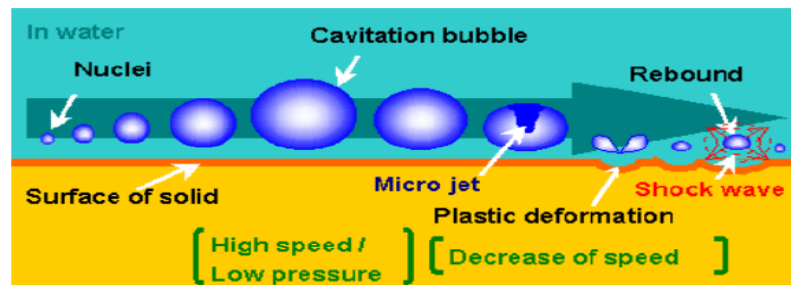


Figure 4.2: Cavitation process [3]

#### 4.4.2. Types of macroscopic cavitation and effects

Mainly three types of cavitation can be found which are travelling isolated bubbles, attached cavities (stable sheet or unstable cloud), and vortex cavitation [1].

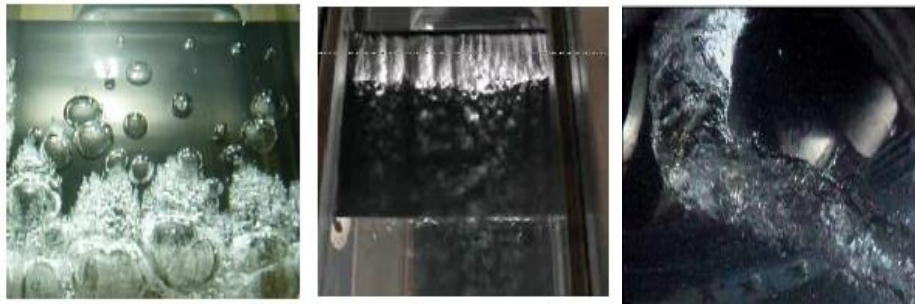


Figure 4.3: Types of cavitation: bubbles, attached and vortex respectively [1]

When cavitation appears then vibrations, erosion and others unwanted phenome can appear in the flow.

#### 4.4.3. Sigma coefficient

The sigma coefficient is a dimensionless parameter which is used to characterize the cavitation in a flow.

$$\sigma = \frac{P_{ref} - P_v}{\frac{1}{2} \rho V_{ref}^2} \quad (\text{Eq. 4.10})$$

Where  $P_v$  is the vapour pressure.

## 4.5. Hydroelectric energy

### 4.5.1. The future of the energy

The world population growth, the industrialization, the improvement of life conditions in developing countries, the increase of the oil price and the climate change are the main humanity's challenges. Moreover, the consume of primary energy of a country is linked to its economy. Thus in 2035, the electricity demands will be 68 per cent higher than in 2011 [2].

The energy coming of fossil fuel produces  $\text{CO}_2$ , enhances the greenhouse effect and the global warming, and it generates more particulates like HC,  $\text{NO}_x$  and  $\text{SO}_2$ . On the other hand, the energy coming from nuclear systems produces hazardous waste. For this reasons, the humanity will have to bet for the renewable energies.

### 4.5.2. Hydroelectric power source

The renewable energy based on hydropower allows saving oil and coal and does not produce greenhouse gasses or other air pollution. Moreover, it also helps to manage the energy due to its quickly starting, that allows meeting peak demands, and the capacity of storage energy when the consummation is low, in pumped storage plants. In conclusion, the hydropower allows adapting the generation to the demand.

The origin of the hydroelectric energy is the natural water cycle and the energy source is the sun. Water acquires potential energy under the action of the energy received from the sun.

Solar radiation incident in large masses of water causes the evaporation of it. Humid air is transported by atmospheric currents (wind) to other regions where it colds down provoking the condensation of vapour, with the aid of airborne particles. When the nucleated (condensed) water forming the clouds achieves enough volume and velocity to avoid evaporation, rainfall appears [2].

When rain water falls on elevated terrain, forms water streams that flow onto lower elevations which are used in the hydroelectric plants. Water resulting from snow and ice meltdown is used too.

#### 4.5.2.1. Types of hydroelectric power plants

There are two different ways to reach a large height difference (potential energy), which have been associated two types of hydroelectric plants.

Run-of-the-river plants use water as it flows in the river and to get a large difference in height between the river and the channel, the plant drives a water flow through a lateral channel with a jump.

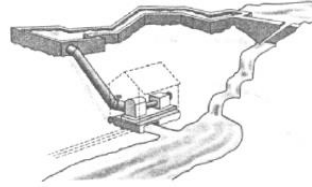


Figure 4.4: Run-of-the-river plant [2]

Reservoir hydroelectric power plants use regulated water by a reservoir and they obtain the difference in the level raising the up-flow water by means of dam. In this group, the regulation plants (which only produce power) and pump-storage plants (which generally can storage energy using a pump system and produce energy using turbines) can be found.

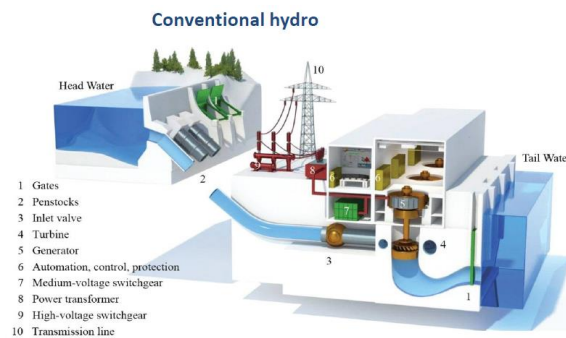


Figure 4.5: Reservoir plant [2]

The reservoir hydroelectric plants can be classified depending on the height difference with high head plants (200 m), medium head plants (20-200 m) and low head plants (lower than 20 m). A full explanation can be found in [2].

#### 4.5.2.2. The hydraulic turbines

The hydraulic energy is converted to electric energy through a system made up by two machines, the turbine and the generator.

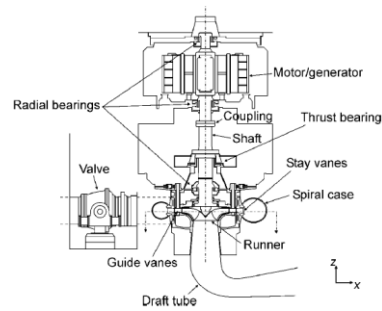


Figure 4.6: The machine [1]

As it is shown in the figure 4.6 the most important parts is the turbine, which transforms the mechanical energy of water into rotational mechanical energy of the runner. Then, other components are the generator, which converts the mechanical energy to electrical energy, and the draft tube, which converts the remaining part of the kinetic energy at the runner outlet to pressure energy increasing the cross section area in the flow direction.

Here below, the different type of turbines are described briefly. A full explanation can be found in [1-3].

#### 4.5.2.2.1 Impulsion turbines

In this type of turbines, the pressure of water is transformed in velocity, the jet of the water losses its kinetic energy in the buckets and there is not drop pressure across turbines.

##### 4.5.2.2.1.1 Pelton

The Pelton is used in high heads (more than 200 m) and low flow rates (less than  $10 \text{ m}^3/\text{s}$ ). It has a good efficiency for a large range of flows (between 30 per cent and 100 per cent of the maximum flow) [2].



Figure 4.7: Pelton [2]

##### 4.5.2.2.1.2 Michell-Banky

Through the gate, the water enters and circulates two times through the blades raising the friction and for this reason the efficiency is smaller than other types of turbines. They can operate in a large range of flow.

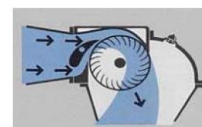


Figure 4.8: Michell-Banky [2]

#### 4.5.2.2.1.3 Turgo

It is a modification of the Pelton turbines converting the buckets into blades. In this turbine, the water can flow in a lot of blades at the same time.

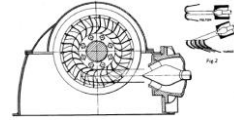


Figure 4.9: Turgo [2]

#### 4.5.2.2.2 Reaction turbines

This type of turbine is submerged in water, the pressure of water acts directly on the blades, there is a pressure drop across turbine and the momentum is converted to shaft power.

##### 4.5.2.2.2.1 Kaplan

It is used in low heads (less than 50 m) and medium to large flows (more than 15 m<sup>3</sup>/s). The efficiency is good for a wide range of flows. They have variable blade orientation.



Figure 4.10: Kaplan [3]

##### 4.5.2.2.2.2 Francis

It can be used in a wide variety of flows (between 2 m<sup>3</sup>/s and 200 m<sup>3</sup>/s) and medium heads. They have a good efficiency for a narrow range of flows (between 60 per cent and 100 per cent of the maximum flow).



Figure 4.11: Francis turbine [2]

The main parts are:

- Spiral case: distributes the pressurized water through the periphery of the set runner-gates by decreasing cross section in order to keep velocity constant.
- Draft tube: joints the runner outlet to the discharge. It recovers the kinetic energy of water, which leaves the turbine at high velocity.
- Wicket gates: distribute flow homogenously in the runner.
- Guide vanes: they are articulated, so that the flow rate can be regulated and the working point of the turbine can be controlled (power output).

- Runner: where the hydraulic energy is converted in mechanical energy.

#### 4.5.2.3. Output power and specific speed

The power given by a hydroelectric plant can be determined like it is shown here below. Using the principle of the potential energy, the theoretical power of the plant can be calculated:

$$P_t = \gamma H_G Q \quad (\text{Eq. 4.11})$$

Where the  $\gamma$  is the specific weight of the water (9810 N/m<sup>3</sup>), and the  $H_G$  the gross head of the plant.

From the theoretical power the mechanical power can be determined:

$$P_m = \gamma H_N Q \eta_t \quad (\text{Eq. 4.12})$$

Where the turbine efficiency ( $\eta_t$ ) is considered to account for the friction losses (heat generation) and the fraction of the water that not circulate through the runner (mass losses). Moreover, the net head is used ( $H_N$ ) instead of the gross head.

Finally, considering the generator's efficiency ( $\eta_g$ ), the electric power given by the plant can be calculated.

$$P_e = \gamma H_N Q \eta_t \eta_g \quad (\text{Eq. 4.13})$$

One of the most important parameters to design a hydroelectric plant is the specific speed that is defined by the next equation:

$$n_s = n P^{0.5} H^{\frac{-5}{4}} \quad (\text{Eq. 4.14})$$

Where  $n$  is the synchronism speed in rpm,  $P$  the turbine power in CV and  $H$  the head in m.

So, the turbine selected for a given hydroelectric plant can be chosen using the next graph (head and specific speed) to maximize efficiency.

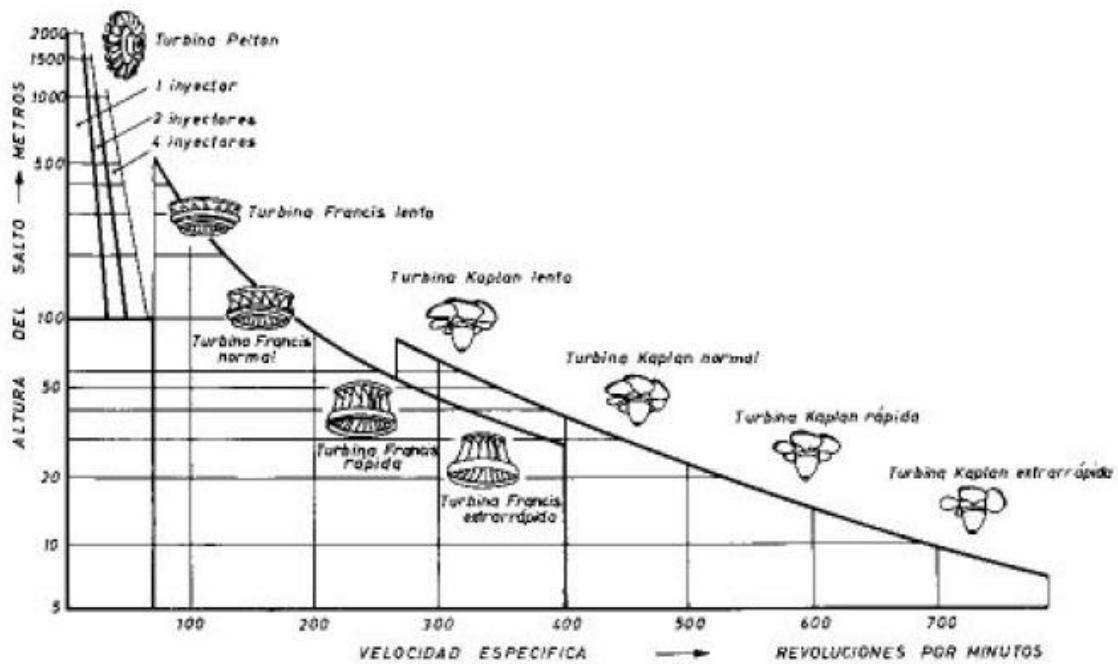


Figure 4.12: Selection turbine graph [2]

## 4.6. Hill chart of an hydraulic turbine

In this section, a brief description about how the turbine can capture energy from the water that circulates through the runner from the theoretical viewpoint will be given.

Two different theories can be applied in order to be able to determine the energy captured by the turbine. Both use the same concept which is to compute the energy inlet and outlet of the runner claiming that the difference is the energy captured by the turbine. However, the principle used to compute the energy is different.

### 4.6.1. Bernouilly

Using this formulation, the energy is calculated applying the Bernoulli's principle between the outlet and inlet of the runner like it can be seen in the next equation:

$$E = \frac{C_1^2 - C_2^2}{2} + g(Z_1 - Z_2) + \frac{P_1 - P_2}{\rho} \tag{Eq. 4.15}$$

Where C is the average absolute velocity, P is the average pressure, Z is the height, E is the specific energy and 1-2 are the inlet and outlet respectively.

This principle needs to have measurements of the velocity and the pressure in the turbine to calculate the energy captured. However, using the Euler principle measurements of the pressure are not needed saving time and money.

#### 4.6.2. Euler

The Euler's formulation is the most fundamental equation in the field of the turbo-machinery since it governs the power and the efficiencies of them. Moreover, using this equation, the given head can be easily determined. This formulation is based on the conservation of the angular momentum [3].

$$\Sigma \vec{M} = \frac{\partial}{\partial t_{cv}} \int r_x \vec{V} \rho dV + \int_{A_e} r_x \vec{V} d\dot{m}_e - \int_{A_i} r_x \vec{V} d\dot{m}_i \quad (\text{Eq. 4.16})$$

The equation 4.16 announces that the sum of all the external moments acting on the control volume is equal to the difference between the rate of change of the angular momentum between the outlet and the inlet surfaces plus the rate of change of the angular momentum inside the control volume which can be considered zero for steady-state conditions. A full explanation can be found in [3].

The Euler equation can be simplified to the below expression which permits to calculate the specific energy through the runner.

$$E = U_1 C_{1u} - U_2 C_{2u} \quad (\text{Eq. 4.17})$$

Where U is the circumferential velocity at the runner inlet and  $C_u$  is the projection of the absolute velocity on the tangential direction.

Knowing that the absolute velocity C is the sum of the circumferential velocity, U, plus the relative velocity W, the next equation can be easily deduced:

$$UC_u = \frac{1}{2} (C^2 + U^2 - W^2) \quad (\text{Eq. 4.18})$$

Where W is the relative velocity and which allows rewriting the equation 4.17 like:

$$E = \frac{C_1^2 - C_2^2}{2} + \frac{U_1^2 - U_2^2}{2} + \frac{W_2^2 - W_1^2}{2} \quad (\text{Eq. 4.19})$$

Which can be related easily with the Bernoulli's formulation since the sum of the second term plus the third term corresponds to the Bernoulli's difference of pressure if the difference of heights is negligible.

### 4.6.3. Characteristics curves

The characteristic curves of a hydraulic turbine can be defined mainly by two dimensionless parameters.

1. Flow coefficient:

$$\varphi = \frac{Q}{\pi \omega R_{ref}^3} \quad (\text{Eq. 4.20})$$

Where  $R_{ref}$  is the reference radius,  $Q$  the discharge and  $\omega$  the angular velocity of the turbine.

2. Head coefficient:

$$\psi = \frac{2gH}{\omega^2 R_{ref}^2} \quad (\text{Eq. 4.21})$$

Where  $H$  is the head of the turbine.

These variables are used to draw the Hill Chart that describes the full operation range of a given turbine with its efficiency for each possible flow condition:

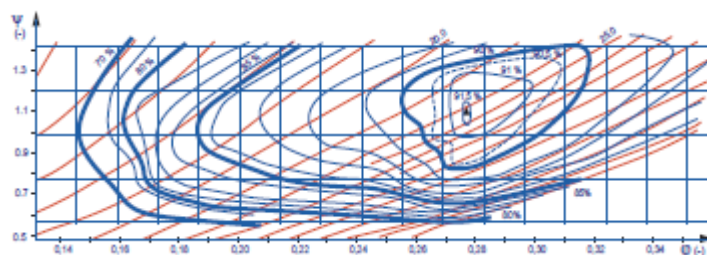


Figure 4.13: Typical hill chart of Francis turbine [6]

## 4.7. Modelling the equations of flow

### 4.7.1. Difficulties solving the equations

In this section a brief explanation about the problems to solve the Navier-Stokes equations in turbulent flows will be given. For more information see the reference [17].

From the Navier-Stokes equations, specifically from equation 4.8, and considering that the external forces are negligible, three equations can be obtained, one for each axis. Moreover, if the fluid is incompressible, one equation more is obtained, from equation 4.9. Finally, the fifth equation is directly the conservation of the mass in the absence of mass' sources, the equation 4.9. For a laminar flow these five equations obtained permits to calculate five unknowns (velocity field, pressure and density).

However, when the flow is turbulent a Reynolds decomposition, which considers the mean and the fluctuation components of the instantaneous property values, must be considered which compromises the solution of the system. Such fluctuations are incorporated in the Navier-Stokes' equations and then they must be average for simplification. The second and the third equations explained above are lineal, however, the first equation is not lineal, thus a new equation is obtained like it can be seen here below [17].

$$\rho \left[ \frac{\partial U_i}{\partial t} + U_j \frac{\partial U_i}{\partial x_j} \right] = - \frac{\partial P}{\partial x_i} + \frac{\partial}{\partial x_j} [T_{ij}^{(v)} - \rho \langle u_i u_j \rangle] \quad (\text{Eq. 4.22})$$

Where the second term in the square brackets on the right is called the Reynold stress tensor which has dimensions of stress and which contributes to the non-linear acceleration terms. As a result six new unknowns appear:  $U_1^2$ ,  $U_2^2$ ,  $U_3^2$ ,  $U_1U_2$ ,  $U_1U_3$ ,  $U_2U_3$ .

Without a doubt, the Reynold stress makes the solution to the turbulence difficult since the averaged equations are not closed and the simplest ideas to provide the extra equations usually do not work. For this reason, a turbulent model is necessary to solve the problem which must be selected carefully.

To solve the Turbulence Closure Problem, the best approach is to try to derive dynamical equations for Reynold stresses from the equations which govern the fluctuations themselves. However, more unknowns than equations always appear. So, it can be concluded that the closure problem cannot be solved by a generic law. Only understanding how the turbulence behaves one can get an appropriate set of equations which limit must be well known.

### 4.7.2. Computational Fluid Dynamics (CFD)

CFD is a branch of Fluids Mechanics which studies different ways of to obtain a solution of Navier-Stokes equations using numerical methods.

If the flow is laminar it is reasonable to solve the full set of Navier-Stokes equations to predict the flow. However, if the Reynolds number is high, the flow oscillates and a turbulent flow is gaining importance up to very high Reynolds numbers when the flow is fully turbulent and exhibits a chaotic variation in time. In this situation, the Navier-Stokes equation cannot be solved directly, as it has been discussed above. For this reason Reynold Average Navier-Stokes (RANS) turbulence models have been developed which predict the time-averaged solution of flow giving approximate solutions.

Moreover, the turbulent flow does not only affect to the solution of the Navier-Stokes equations, it also alters the heat transfer and the mass diffusion including additional parameters to simulate the effect of turbulence.

Although the flow can be classified like turbulent, near the wall the flow can be divided into three flow regimes [16]:

- Viscous sublayer (approximately laminar), close to the solid boundary.
- Buffer layer (between the sublayer and the turbulent region).
- Turbulent region (far from the wall).

To solve the flow in these regions, the numerical methods have two options:

- Using analytic wall functions which compute the boundary condition at the end of the buffer layer.
- Without wall functions, so the flow is solved all the way to the wall. But it requires a much finer mesh and many more elements are needed to resolve the flow in the viscous sublayer.

The most important RANS turbulence models available in CFD are [17]:

- Spalart-Allmaras, which was developed for aerodynamics studies. It is stable and uses less memory than Low Re K-epsilon and SST. It does not use wall functions, thus accurately computes forces (lift and drag) and flux (heat and mass transfer). However, it does not accurately compute flow fields which exhibit shear flow, separated flow or decaying turbulence.

- K-epsilon, which uses wall functions and thus a coarse mesh near the wall can be used. It performs well for external flow problems and complex geometries. On the other hand, due to the wall function approximation, solution at wall is less accurate and it does not accurately compute flow fields which exhibit adverse pressure gradients, strong curvature of flow and jets.
- K-omega, which requires the same memory than k-epsilon and it performs well for internal flow problems and fields with curvature, separated flows and adverse pressure gradients. However, due to the wall function approximation, the solution at wall is less accurate. The model is sensitive to free stream. Often, the k-epsilon model is used to find an initial condition for a more accurate simulation.
- The low Re K-epsilon, which is a logical extension of the K-epsilon model, and often runs subsequently to get higher accuracy solution. Moreover, it does not use wall functions, thus obtaining more accurately results. However, this model requires finer mesh in the boundary layer and use more memory than k-epsilon and k-omega.
- The Shear Stress Transport (SST), which tends to be most accurate for solving the wall flow because it combines k-epsilon model in the free stream and k-omega model near the wall and does not use wall functions. On the other hand, this model requires care in selecting initial conditions at higher Reynold numbers and the boundary layer mesh must be very fine. It is not accurate for swirling flows and it uses more memory than K-epsilon and K-omega.
- The Algebraic yPlus and L-VEL models, which are suitable for internal flows. They are more robust than other turbulence models, use short memory and using them is possible to obtain accurately computes because they do not use wall functions.

## 5. Cavitation in turbines

### 5.1. Cavitation numbers

The most important parameters to understand the cavitation in the turbines will be explained in this section.

The Net Positive Suction Energy (NPSE) is the difference between the specific energy at section 2 (see Fig. 5.14) minus the specific energy associated to the vapour pressure  $P_v$ , referred to the reference level of the machine [6].

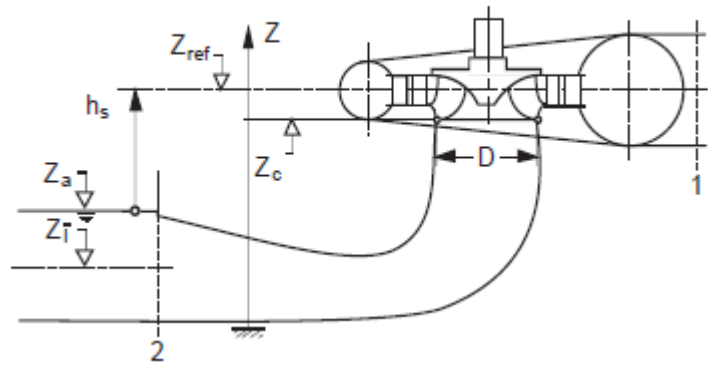


Figure 5.14: Turbine's scheme [6]

Thus the NPSE, where  $H_2$  is the available total head in section 2, is determined by:

$$NPSE = gH_2 - \frac{P_v}{\rho} - gZ_{ref} \quad (\text{Eq. 5.23})$$

For a turbine, where  $P_a$  is the atmospheric pressure at the exit section, it can be simplified:

$$NPSE \approx \frac{P_a}{\rho} - \frac{P_v}{\rho} - gh_s + \frac{C_2^2}{2} \quad (\text{Eq. 5.24})$$

Another two important parameters to understand better the NPSE and the variables explained below are the setting level:

$$h_s = Z_{ref} - Z_a \quad (\text{Eq. 5.25})$$

And the specific energy:

$$E = gH_1 - gH_2 \quad (\text{Eq. 5.26})$$

Using the NPSE, two important dimensionless cavitation numbers can be defined, the Thoma number [6]:

$$\sigma_T = \frac{NPSE}{E} \quad (\text{Eq. 5.27})$$

Such as it can be seen in the above equation, the Thoma number is an adaptation of the sigma coefficient for hydraulic turbines.

And the net specific energy coefficient [6]:

$$\psi_c = \frac{2NPSE}{\omega^2 R_{ref}^2} \quad (\text{Eq. 5.28})$$

As discussed above, one of the most important parameter to avoid the cavitation in the hydroelectric plant is the setting level. Let us not forget that there is a trade-off between the cost of the installation and the level of the turbine.

To facilitate the calculation of the recommended setting level based on the specific speed (Eq. 4.14), the next graph can be used:

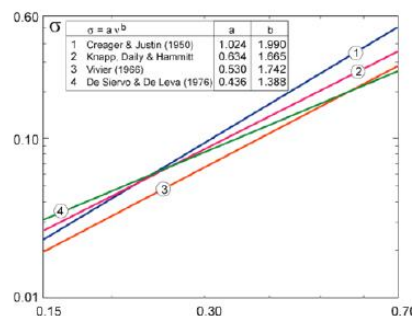


Figure 5.15: Critical Thoma number graph as a function of  $ns$  [1]

With the acceptable Thoma number to avoid the cavitation, the NPSE and then the highest

$h_s$  can be found.

On the other hand, the Thoma number and the specific energy coefficient allow explaining other parameters to understand the cavitation better.

As discussed above, these two numbers are easily determined since they are only related with the setting level, however for the study of the cavitation the static pressure in the low-pressure (runner's outlet) section should be known. Using the variables defined above and applying the energy conservation between the section C and the section 2, the local cavitation factor can be determined [6]:

$$\chi = \frac{P_C - P_v}{\rho E} = \sigma_T + \frac{1}{F_r^2} \left( \frac{Z_{ref} - Z_c}{D} \right) - \frac{C_c^2}{2E} + e_{rd} \quad (\text{Eq. 5.29})$$

Where  $e_{rd}$  is losses coefficient and  $F_r$  is the Froude number, which depends of  $E$ ,  $D$  and  $g$ .

The local cavitation number can also be expressed as a function of the discharge coefficient, where  $\varphi_0$  is the discharge operation with minimum whirl [6]:

$$\chi = \sigma_T + \frac{1}{F_r^2} \left( \frac{Z_{ref} - Z_c}{D} \right) - \frac{\varphi^2 + (1 - \frac{\varphi}{\varphi_0})}{\psi} + e_{rd} \quad (\text{Eq. 5.30})$$

From equation 5.30, the strong relation between the static pressure in section C and the discharge coefficient, even though the Thoma number is kept constant, can be seen.

On the blade of the turbine acts forces which generate a moment on the axis of the turbine called torque. The origin of all these forces is mainly the pressure. Thus a specific pressure coefficient for turbines has been defined.

$$C_{Pc} = \frac{P - P_c}{\rho E} \quad (\text{Eq. 5.31})$$

The necessary condition for the onset of cavitation would be  $C_{Pc} = -\chi$ .

And from equation 5.30, the increase of discharge until the pressure in section C decrease up to reach the pressure vapour,  $\chi = 0$ , can be deduced [6].

If the pressure in section C is the vapour pressure, the reference at the runner outlet is taken, the losses are neglected and a whirl free condition is assumed, the local cavitation number would be [6]:

$$\chi = 0 \approx \sigma_T - \frac{\varphi^2}{\psi} \quad (\text{Eq. 5.32})$$

From the equation 5.32 was born the margin to vapour pressure (K):

$$K = \frac{\psi_c}{\varphi^2} \quad (\text{Eq. 5.33})$$

and to avoid cavitation, the K should be bigger than 1,8 [6].

To understand better the turbine's operation for each working point the next curve can be plotted.

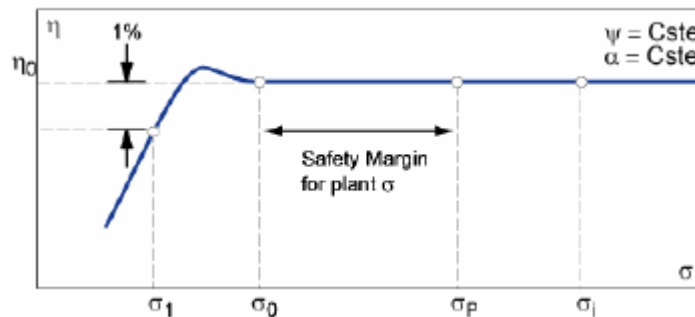


Figure 5.16: Cavitation graph [6]

Where the head, torque or efficiency change according to the Thoma number. The cavitation inception number,  $\sigma_i$ , indicates the onset of cavitation but until  $\sigma_0$  is not reached the efficiency remains unchanged.

## 5.2. Cavitation in Francis turbines

As discussed in section 4.4.2 the cavitation can lead to unwanted consequences. Measurement's errors and efficiency's drop can appear due to the lock of the liquid's cross-section pass, apart from sounds, vibration or erosions due to the cavitation's collapse. All this coupled with instabilities limit the area of work of the turbines. For this reason, it is so important to know when and where cavitation appears.

Mainly two types of cavitation can be found in turbine's runners [6]:

- Blade leading edge cavitation: the onset of leading edge cavity is more influenced by the blade geometry and the flow incidence angle than the Thoma number. For this reason, prevent this type of cavitation will cause unacceptable costs and cannot be avoided for off-design operation.
- Bubble cavitation: the onset of a cavity is due to the design operation point which is very sensitive to the Thoma number.

In case of Francis turbines, the development of the cavitation is strongly related with the energy coefficient whereas the flow coefficient influences only the whirl cavity at the draft tube [6].

- When the energy coefficient is increased or reduced cavitation appears at the leading edge suction and pressure sides of the blade respectively. This type of cavitation is very dangerous for the machine and it is not sensitive to the Thoma number (Blade leading edge cavitation) [6].
- On the other hand, when the turbine is operating in the design point, with low angles of attack, travelling bubbles will appear which are very sensitive to the Thoma number and to the content of nuclei (Bubble cavitation) [6].

To be able to see the drop of the torque and the efficiency of the turbine, both types of cavitation have to be highly developed.

The value of the flow coefficient is highly related with the developed shape and whirl of the cavity from the hub of the runner to the centre axis of the draft tube and the size of the cavity is dependent of the Thoma number [6] like it can be seen in the next figure.

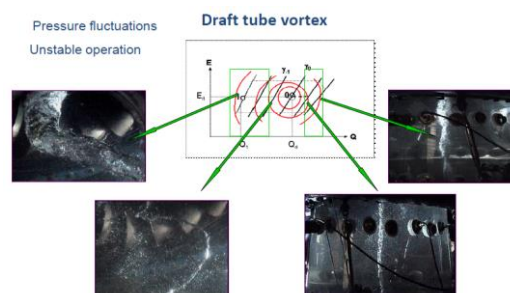


Figure 5.17: Vortex cavitation [1]

In Fig. 5.17, it is shown that high flow rate leads to a large axi-symmetric fluctuating cavity, whereas low flow rate leads to a helical shape of the whirl according to the direction and

magnitude of the outlet absolute velocity [6].

When the vortex cavity increases a lot, due to the partial load off-design operation, it can extend up to the blade to blade passage obstructing the pass of the fluid and provoking a flow recirculation at the inlet [6].

In the next chart, the different types of cavitation, which can appear when the operation point is moved in the hill chart, are shown.

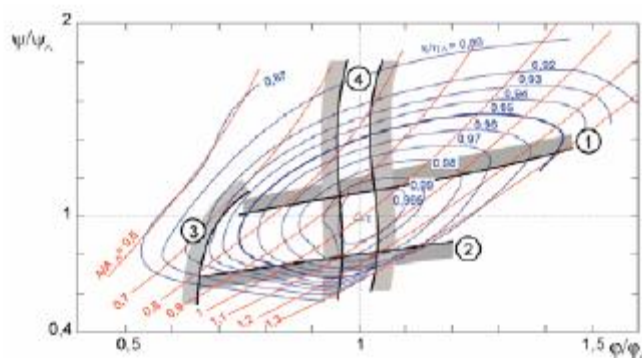


Figure 5.18: Cavitation limits [6]

Where 1 is the suction side leading edge cavitation limit, 2 is the pressure side leading edge cavitation limit, 3 is the interblade cavitation vortices limit, and 4 is the discharge swirl cavitation limit [6].

Traveling bubble cavitation is strongly sensitive to the content of the cavitation nuclei (cavitation inception) and the Thoma number, for this reason the plant's NPSE is determined with respect this type of cavitation [6].

However, the cavitation nuclei content also influences the development of bubble traveling cavities [6]. Thus, it also influences the efficiency alteration. For this reason, to know the number of active nuclei is so important.

According to the Rayleigh-Plesset, the activity of nuclei is directly dependent on the radius of the active nucleus which depends on the head of the turbine [6].

In conclusion, the efficiency alteration is due to the vaporization of the water and it depends on the amount of vapour that forms between blades (inside the runner channels). In order to disturb the efficiency, enough active nuclei are needed inside the runner channels [6].

### 5.3. The Rayleigh Plesset Model

In this section, the Zwart-Gerber-Balamri (ZGB) cavitation model that will be used in the numerical model of the runner is briefly described and its relation with the Rayleigh Plesset equation is explained. For more information Ref. [20] can be consulted.

The mass transfer between the liquid water and the vapour water during the cavitation process, using the ZGB model, can be determined from the Rayleigh Plesset law of nuclei growth given by the following equation:

$$R_B \frac{d^2 R_B}{dt^2} + \frac{3}{2} \left( \frac{dR_B}{dt} \right)^2 + \frac{2\sigma}{\rho_f R_B} = \frac{P_v - P}{\rho_f} \quad (\text{Eq. 5.34})$$

In the next figure, the evolution of the radius of the bobbles is described by the Rayleigh Plesset equation.

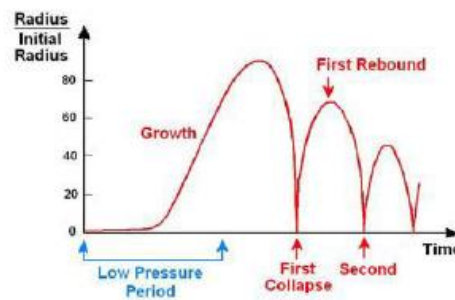


Figure 5.19: Rayleigh Plesset equation [3]

And the equation used by the ZGB model is found neglecting the second order terms, where  $\rho_f$  is the density of the liquid:

$$\frac{dR_B}{dt} = \sqrt{\frac{2(P_v - P)}{3\rho_f}} \quad (\text{Eq. 5.35})$$

Using Eq. 5.35, the change of nuclei's volume can be easily determined, multiplying it by the density of the vapour ( $\rho_g$ ). And using the vapour volume fraction ( $r_g$ ), the change of mass with time can be found.

$$\dot{m}_{fg} = \frac{3r_g \rho_g}{R_B} \sqrt{\frac{2(P_v - P)}{3\rho_f}} \quad (\text{Eq. 5.36})$$

A constant  $F$  can be defined that is set differently depending if the vaporization (in the elements where  $P$  is lower or equal than  $P_v$ ) or if the condensation (in the elements where  $P$  is greater than  $P_v$ ) takes place. Usually, the vaporization is much faster than the condensation. Then, two different equations, which describe the mass of vapour shifted to liquid or vice versa, can be obtained.

To obtain the vaporization mass rate some more change have been made like it can be seen in Eq. 5.37.

$$\dot{m}_{fg} = F \frac{3r_{nuc}(1-r_g)\rho_g}{R_{nuc}} \sqrt{\frac{2(P_v - P)}{3\rho_f}} \quad (\text{Eq. 5.37})$$

Where  $R_{nuc}$  is the nucleation site radius (nuclei's radius) and  $r_{nuc}$  is the volume fraction of the nucleation site (amount of nuclei).

## 6. Computational Model

### 6.1. The GAMM Francis turbine

Turbine geometry and performance measurements are typically confidential in the hydropower industry. However, a particular turbine design has been chosen because it is an open case that has already been investigated by the scientific community.

The GAMM Francis turbine model was built and tested experimentally at the IMHEF which is a hydraulic laboratory in Lausanne, Switzerland. Then, the numerical results were presented in a workshop on 3D computational of incompressible internal flows in 1989, and in ERCOFTAC seminar and workshop on turbomachinery flow predictions in 1995. Although, several off-design conditions measurements have been made, this thesis is focused in the study of the Best Efficiency Point (BEP).

#### 6.1.1. Geometry

In this section, the principal geometric characteristics of the GAMM Francis turbine are described.

The runner has 13 blades, a specific speed of 0,5 and an external diameter of 0,4 m. For this reason, the reference radius is set to 0,2 m. The distributor has 24 stay vanes and 24 guide vans, and the draft tube has a simple design.

#### 6.1.2. Test measurements

To get a good simulation it is important to know where and how the variables used to impose the boundary conditionals have been measured.

The pressure and velocity distribution were measured using a 6 mm diameter five-hole pressure probe, which gives the three components of the local flow and the local static pressure. These measures were made at the inlet of the distributor, at the inlet of the runner blade (which is the measure used in this thesis), at the inlet of the draft tube and at the outlet of the draft tube. In others parts such measurements were not made due to flow instabilities [9]. Moreover, the pressure distribution on the runner blades along three profiles of the blades was obtained with pressure transducers. Next figure shows the exact localization where these measurements were made.

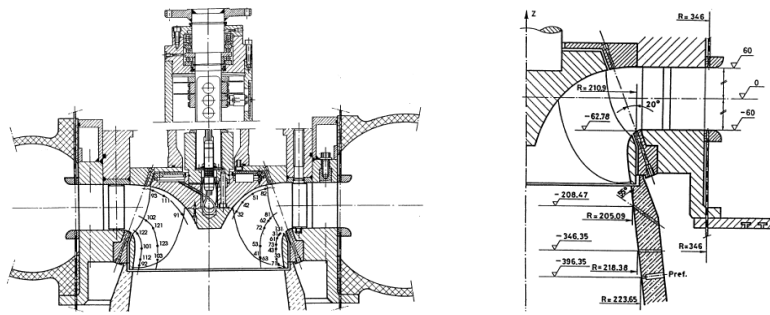


Figure 6.20: Vertical cut of the GAMM Francis [9]

The specific energy between the inlet section of the turbine and the reference section in the diffuser was also measured and the hill chart was obtained.

However, the objective of the current project is to simulate the operation at the BEP, where the flow coefficient is 0,286 (flow rate of 0,372 m<sup>3</sup>/s), the heat coefficient is 1,07, the efficiency is 0,92, the torque is 388 Nm and the rotational speed is 52,36 rad/s. In the Fig. 6.21, the BEP point is indicated with number 1.

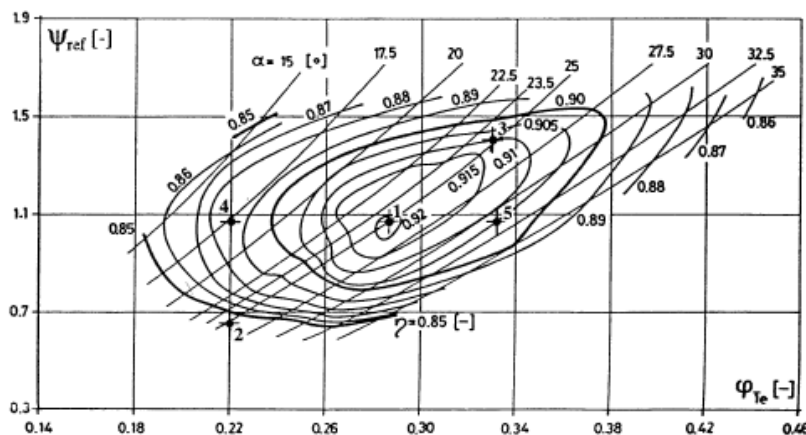


Figure 6.21: Hill chart of the GAMM Francis [9]

## 6.2. Computational domain

The smallest part of the whole runner geometry that permits to obtain complete results must be identified and simulated in order to increase speed computer and use less memory. The GAMM Francis turbine geometry has been able to be simplified applying symmetries thanks to the rotating periodicity of the domain.

In this thesis two different models have been used, one where entire domain will be static

and another where three different domains will be used and one of them will rotate. Here below the procedure to obtain these two models is explained.

The geometry of the runner with only one blade had been provided to us. However, this raw geometry of the turbine had to be manipulated to make the entire computational domain. All realized operations to get the final computational domain have been made with SolidWorks®. In the next figure, three pictures show the runner geometry.

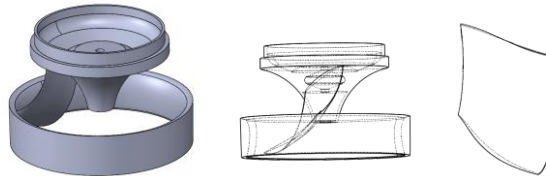


Figure 6.22: Raw Geometry of GAMM

The picture on the left shows holes at the upper centre part of the turbine that have been solidified in order to obtain the fluid domain. The picture on the right shows only one blade, which will be revolutionized to obtain the entire runner.

Knowing that the turbine has 13 blades and using a matrix operation, setting an equal distance between each blade, the entire turbine has been obtained. Then, the centre cavities have been solidified. The result can be seen in Fig. 6.23.

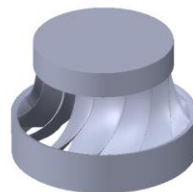


Figure 6.23: The entire GAMM

The simulated domain is the fluid and principally there are two different options to cut it:

- The fluid between two consecutive blades.
- The fluid surrounding one blade between two channels.

The first option is easier to get with SolidWorks®, however, it has complications in the simulations because the results can be more sensible to an imperfect inlet boundary condition. Moreover, the direction of the flow conditions the actions on the blade like the torque or the cavitation.

The second option allows simulating better the effect of the boundary layer on the blade although to obtain the fluid domain is more complicated. Thus the second option has been chosen.

To get the domain, the entire runner, less the used cavity to simulate, has been solidified using surface and cover instructions to fill the rest of the turbine. The result can be seen in Fig. 6.24, which presents a rotational symmetry.

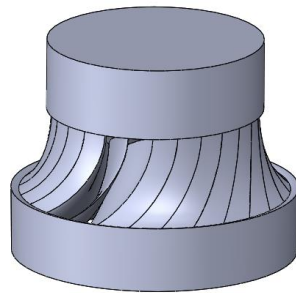


Figure 6.24: Solidified runner

The next step has been to generate a solid, which consists in two cylinders which have been butted through of an arc with the same radius that the border of the runner, like it is shown in figure 6.25, and from which the final domain will be obtained subtracting it from the solid runner previously assembled.

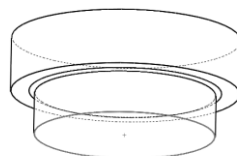


Figure 6.25: The positive solid of the assembling

By subtracting and cutting the external ring while respecting the rotational symmetry, the final domain has been obtained.

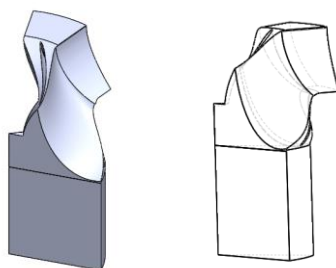


Figure 6.26: The final fluid domain

The extra width, of the external ring, has been fixed to avoid that the inlet boundary conditions influences in the runner. At the outlet of the runner, the exit tube has been extended in order to have a better outlet boundary condition.

### 6.2.1. Computational domain for the stage simulation

To simulate the runner's rotational speed, the domain showed in figure 6.26, has been divided into three parts. The inlet and the outlet are stationary and the intermediate one comprising the runner is rotative. Then, the angular velocity must be imposed to the runner domain.

The main idea to cut the domain correctly is to know what part of the domain is rotating with the runner. To different ways to obtain these cuts are presented. Both ways give the same simulations' results although the picture on the right of figure 6.27 is more realistic [5],[13]. The picture on the left of Fig. 6.27 shows a simpler geometry. However for the current work it converges better, thus the cavitation study has been carried out with it.

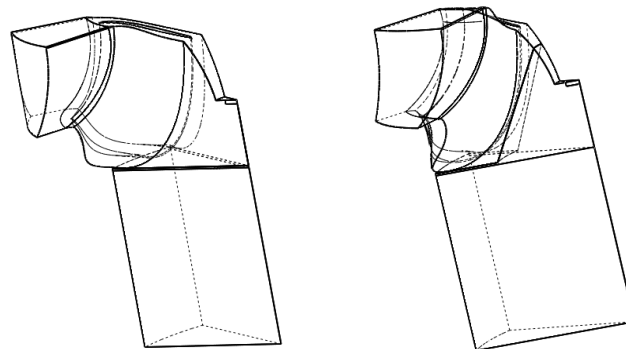


Figure 6.27: The domain of stage simulations

In both cases, the cut made at the inlet of the runner is the same. However, the difference is found at the outlet of the runner. The picture on the left shows that the water between the blades and the centre axis of the runner is rotating.

### 6.3. Mesh

The mesh is one of the most important parts in a simulation since it determines the accuracy of the results.

To get a good mesh, the critical regions where a high number of cells are needed to capture the movement of the fluid because the flow properties present higher gradients have to be identified.

A high number of cells in the mesh increase the computing time. For this reason, regions with less influence on the flow should have a coarse mesh. It allows gaining time and refining the mesh in the interest areas without exceeding the maximum number of elements the computer can handle. On the other hand, sometimes to increase the number of elements does not improve the results after a critical quantity has been achieved.

The computational domain of the GAMM is complex, thus a trade-off between the computational capacity and the number of cells supported by the laptop used to compute is necessary. For this reason, a very refined mesh could not be obtained. Therefore; a mesh sensitive study has been made prior to compute the final solutions.

The Yplus coefficient is used as an indicator about the capacity of the mesh to capture all the effects of the fluid near the wall in the boundary layer. It can be used to determine the height value of the element in contact with the wall. However, to reduce the grid it is feasible to use a RANS turbulence model with wall functions. In this case, a coarse mesh can be used close the wall. If wall functions are not used near the wall, the height of the first cell would be less than  $\Delta y$  [16] as indicated in Fig. 6.28.

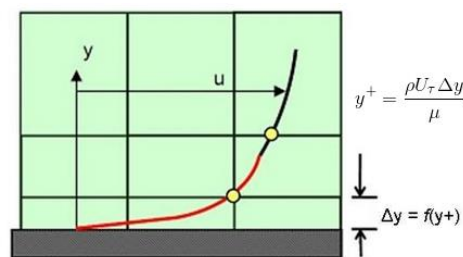


Figure 6.28: The  $y^+$  definition [16]

In the entire computational domain is important to obtain accuracy results, thus only a one type and size of element has been considered. However, one of the most important magnitudes in a turbine is the torque and it is obtained from the forces which act on the blade. For this reason, the mesh has been refined close the blade using an inflation.

### 6.3.1. Static simulation mesh

This mesh has 2165510 elements and 791810 nodes and it is characterized by:

- Tetrahedral elements for the entire domain except the regions close the wall where inflation has been applied.
- Using an advanced sizing on proximity and curvature.
- Max. face size and max. size of 6 mm.

- A general inflation close all surfaces defined as walls, setting the first layer thickness to 0,3 mm, maximum number of layers to 40 and growth rate to 1.

In the next three graphics it can be seen that as the mesh becomes finer the tree main monitored parameters of the simulation stabilize. From the results it can be concluded that the fifth mesh size is enough to obtain accurate results, thus it will be used to simulate.

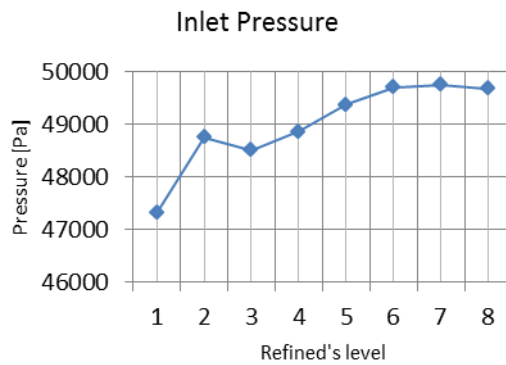


Figure 6.29: Inlet Pressure

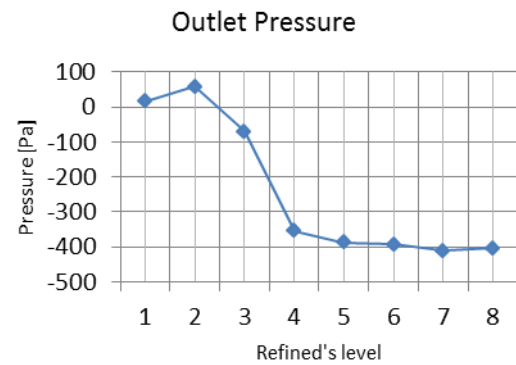


Figure 6.30: Outlet Pressure

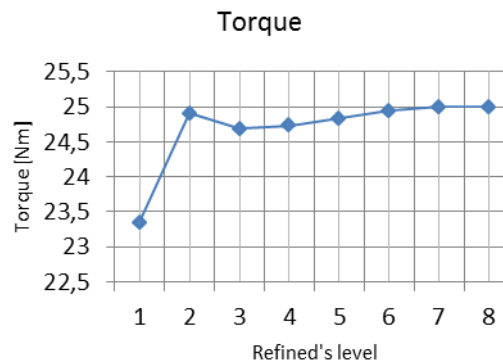


Figure 6.31: Torque

On the other hand, the Yplus values on the blade have also been studied. The results are shown in Fig.32 and although they are high, the mesh quality can be considered good enough.

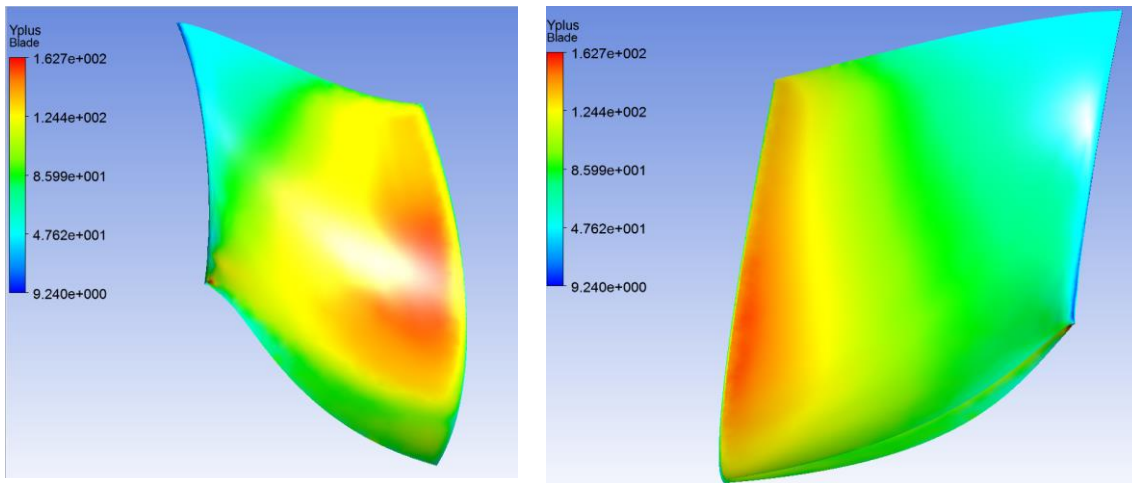


Figure 6.32: The Yplus

In the next Fig. 6.33, a general view of the used mesh and a detail of the inflation are shown.

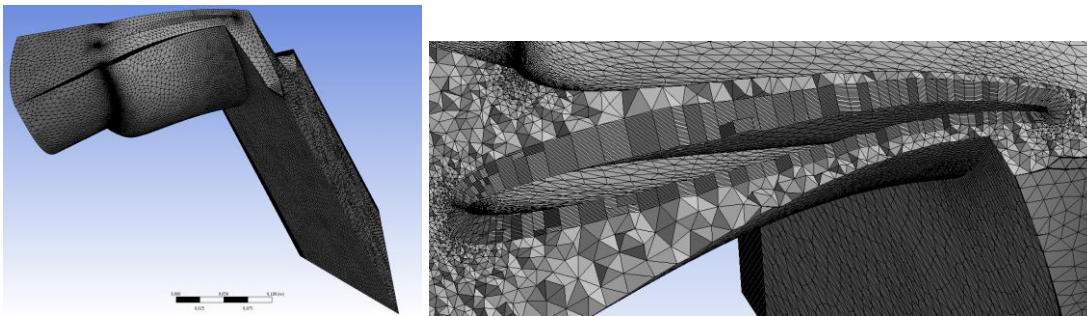


Figure 6.33: The mesh

### 6.3.2. Stage simulation mesh

The mesh has 1854424 elements and 445510 nodes and it is characterized by:

- The main elements are tetrahedrons.
- Advanced sizing on curvature.
- Max. face size and max. size of 3 mm.
- Inflation localized only in the runner domain and close to the blade, setting the first layer thickness to 0,8 mm, the maximum number of layers to 30 and the growth rate to 1,1.

In the next graphs, the torque and the pressure's drop evolution with mesh size are shown and they permit to conclude that last mesh is the most adequate.

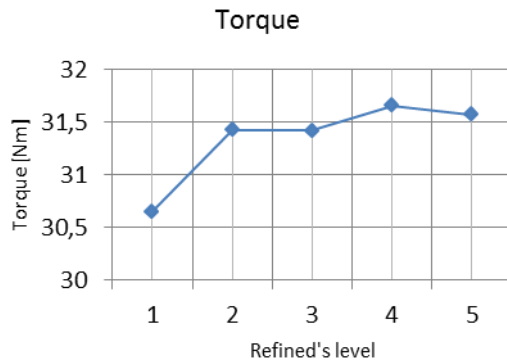


Figure 6.34: Torque

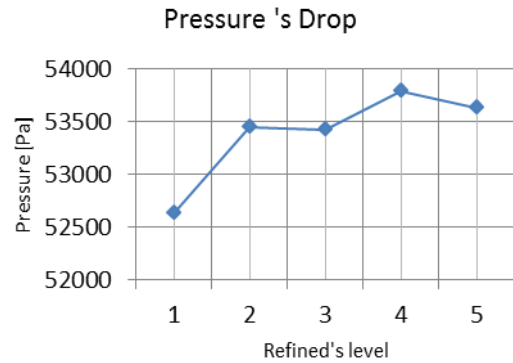


Figure 6.35: Drop pressure

On the other hand, the Yplus results on the blade are shown in the next figure. Likewise in the static study, the results obtained for the Yplus are high, however, they are considered acceptable.

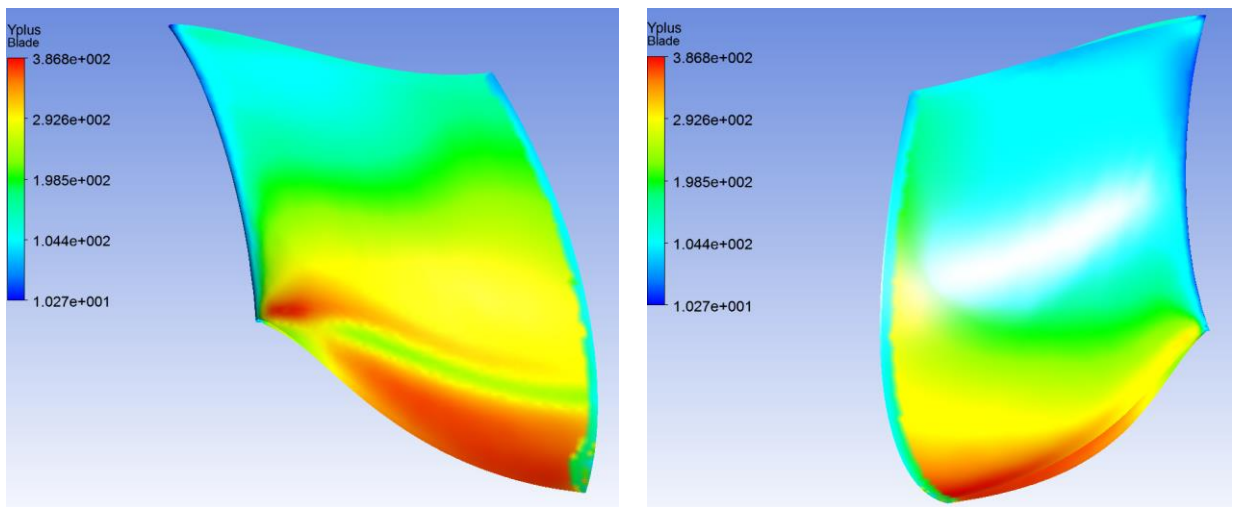


Figure 6.36: The Yplus

In the next figure a general view of the mesh and a detail of the inflation is shown.

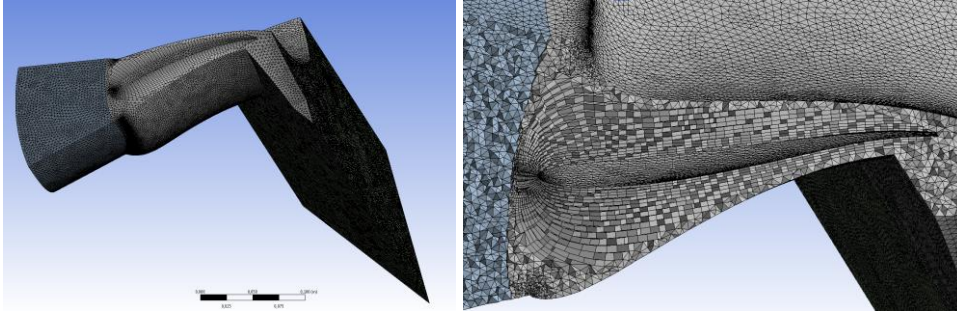


Figure 6.37: The mesh

## 6.4. Turbulence model

Two turbulence models have been considered which can be classified like ‘linear eddy viscosity models’. The K-epsilon model is used to find an initial solution, and the Shear Stress Transport (SST) model is used to find the final solution from the obtained solution with the K-epsilon model.

To understand better the used model, a slightly deeper explanation will be made. More information can be found in [17].

### 6.4.1. The K-epsilon mode

The K-epsilon model appeared to improve the mixing-length model and as an alternative to algebraically prescribing turbulent length scales, giving good results for free-shear layer flows with relative small pressure gradients [17].

It uses two equations, where the K variable is used to determine the energy of the turbulence and the  $\epsilon$  variable is used to determine the scale of the turbulence [17], like it can be seen in Eq. 6.38 and 6.39 respectively.

$$\frac{\partial}{\partial t}(\rho k) + \frac{\partial}{\partial x_i}(\rho k u_i) = \frac{\partial}{\partial x_j} \left[ \left( \mu + \frac{\mu_t}{\sigma_k} \right) \frac{\partial k}{\partial x_j} \right] + P_k + P_b - \rho \epsilon - Y_M + S_k \quad (\text{Eq. 6.38})$$

$$\frac{\partial}{\partial t}(\rho \epsilon) + \frac{\partial}{\partial x_i}(\rho \epsilon u_i) = \frac{\partial}{\partial x_j} \left[ \left( \mu + \frac{\mu_t}{\sigma_\epsilon} \right) \frac{\partial \epsilon}{\partial x_j} \right] + C_{1\epsilon} \frac{\epsilon}{k} (P_k + C_{3\epsilon} P_b) - C_{2\epsilon} \rho \frac{\epsilon^2}{k} + S_\epsilon \quad (\text{Eq. 6.39})$$

### 6.4.2. The shear stress transport (SST) model

This model also uses two equations. It combines the use of K-omega in the inner part of the boundary layer and the K-epsilon formulation in the free stream. It does not use wall functions. This model can be used all the way to the wall avoiding the sensitive problem to the inlet free-stream of K-omega and giving better results.

This model gives good results in adverse pressure gradients and separating flow whereas it produces bit too large turbulence in regions with large normal strain [17].

Mathematically this model is described by the turbulent kinetic energy and the specific dissipation rate equation [17] like it is shown in equations 6.40 and 6.41 respectively.

$$\frac{\partial k}{\partial t} + U_j \frac{\partial k}{\partial x_j} = P_k - \beta^* k \omega + \frac{\partial}{\partial x_j} \left[ (\nu + \sigma_k \nu_T) \frac{\partial k}{\partial x_j} \right] \quad (\text{Eq. 6.40})$$

$$\frac{\partial \omega}{\partial t} + U_j \frac{\partial \omega}{\partial x_j} = \alpha S^2 - \beta \omega^2 + \frac{\partial}{\partial x_j} \left[ (\nu + \sigma_\omega \nu_T) \frac{\partial \omega}{\partial x_j} \right] + 2(1 - F_1) \sigma_{\omega 2} \frac{1}{\omega} \frac{\partial k}{\partial x_i} \frac{\partial \omega}{\partial x_i} \quad (\text{Eq. 6.41})$$

## 6.5. Boundary conditions

To impose the adequate boundary conditions are very important to simulate correctly; although, the boundary conditions are always a simplification of the reality.

### 6.5.1. Boundary conditions for static simulation

This first simulation is a major simplification of the reality and due to that the runner is static the relative velocity has been imposed. In the next figure it is shown where the inlet, outlet and rotational periodicity can be found.

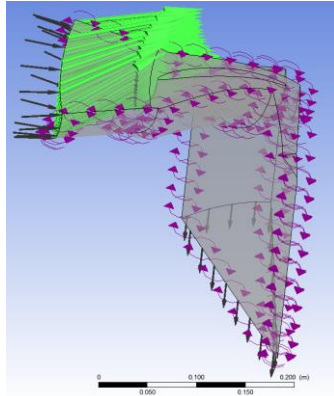


Figure 6.38: Boundary conditions

### 6.5.1.1. General Setting

In this section, the general features of the model have been set:

- Material: Water.
- Morphology: continuous fluid.
- Reference pressure: 1 atm.
- Isotherm: 25°C with a density of 997,38 Kg/m<sup>3</sup>.

### 6.5.1.2. Walls

The SST model has been chosen to solve the turbulence thus wall functions have not been used obtaining more accurately results close the wall but needing a much finer mesh since the flow is solved all the way to the wall.

On the other hand, the velocity of the fluid in contact with the wall is set to 0 with regard to the wall (no-slip).

### 6.5.1.3. Inlet

In this first simulation, a static runner has been simulated thus the relative velocity viewed by the blades had to be imposed.

To simulate the turbine working at the BEP, the radial velocity has been determined imposing that the flow rate is conserved through the cross-pass area. The tangential velocity has been computed from the triangle of velocities imposing a beta angle, or angle between the circumferential velocity and the relative velocity, of 17°. Finally, the axial

velocity has been set to 0.

- Radial velocity = 2,624 m/s
- Tangential velocity = 1,515 m/s

#### 6.5.1.4. Outlet

At the outlet, the relative average static pressure has been set to 0 Pa. In this way, the pressure is not fixed to 0 anyway; instead, the average pressure in this surface should be 0 Pa.

#### 6.5.1.5. Rotational symmetry

To simulate an entire turbine a large computational capacity is needed, thus only a piece of the entire turbine will be simulated. Rotation symmetry has been set in all the faces of the two sides of the fluid domain. On the other hand, due to its orientation, the Y axis has been imposed as the rotational axis.

### 6.5.2. Boundary conditions for stage simulation

The location of the boundary conditions is shown in the next Fig. 6.39.

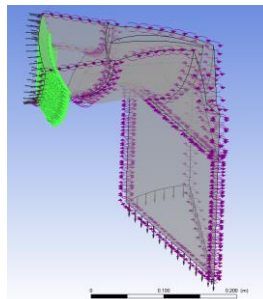


Figure 6.39: Boundary conditions

#### 6.5.2.1. General setting

As discussed in section 6.2.1, the computation model has been cut in three pieces, the inlet and the outlet with a rotational speed of 0 rad/s, and the runner that has a rotational speed of 52,36 rad/s. For the remain parameters, the same general setting that in the section 6.5.1.1 has been imposed.

### 6.5.2.2. Inlet

The velocity field at the inlet of the runner fluid domain, which has been obtained from the bibliography, has been extrapolated to the external inlet boundary surface located at a radius of 252 mm conserving the angular momentum and the mass flow between the runner and the main domain inlets. However, at this boundary the axial velocity has been set to 0 [14],[15].

In the next figure, it is shown the value of the velocity at inlet runner section from the bibliography where  $z$  is the vertical axis of the runner.

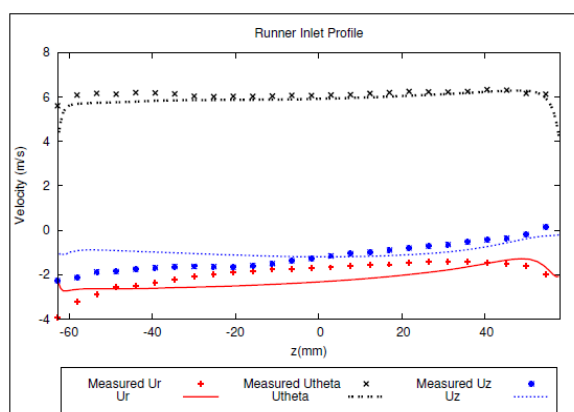


Figure 6.40: Velocity profile at inlet runner section [12]

From the figure 6.40 and applying the explained hypothesis above, the radial velocity and tangential velocity has been set to 1,846 m/s and 4,1 m/s respectively.

### 6.5.2.3. Rotor-stator interaction

To calculate correctly the rotor-stator interaction (RSI) it is necessary to define correctly the coupling between the runner and the stationary fluid domains.

The flow inside a hydraulic turbine is mainly fluctuating, no stationary and it is affected by the interaction between the runner blades and the stationary elements like the guide vanes.

RSI phenomena can be described by relation between the convective time, which is the residence time of one fluid element into the runner, and the characteristic time, which is the characteristic time of the flow perturbation due to the interaction between stationary and rotating elements [5].

In particular, the reduced frequency is described like the ratio between the convective ( $t_c$ ) and the characteristic ( $t_D$ ) time for the axial and radial machines. It can also be described as a function of the number of blades ( $z_t$ ), the rotational frequency ( $n_\omega$ ), the average streamline length ( $l$ ) and the particle's rotational speed ( $\omega_r$ ) [5].

$$\omega_{red} = \frac{l z_t n_\omega}{\omega_r t_D} = \frac{t_c}{t_D} \quad (\text{Eq. 6.42})$$

The reduced frequency is an indicator of the influence of the unsteady effects. If it is less than one, the flow can be considered as steady. Although the reduced frequency is not often small enough, the use of steady-state methods is widely used because they are less costly than transient methods [5].

#### 6.5.2.3.1 Frozen rotor

With the boundary condition named frozen rotor, the stator and the rotor are calculated with different frames of reference and each one is treated like stationary. At their interface, a transformation of reference frame is made between the runner's moving frame and the stationary frame of the statics parts. There is not a relative movement between the mesh of the runner and the stationary ones. This method is robust. However, because the temporal elements of the Navier-Stokes equations are omitted, the inertial force is not taken into account. Thus this method requires care when studying the importance of the inertial forces [5].

#### 6.5.2.3.2 Stage

With this method, all domains of the model (static and rotary) are calculated with stationary reference frame and the coupling between the two contact areas is made through the exchange of average values which are calculated azimuthally in the interface [5]. This method has been used in this work.

### 6.5.3. Boundary conditions for cavitation simulations

For higher turbine setting levels, the pressure at the runner outlet drops and it can provoke the cavitation's onset although the turbine is working at the BEP.

To force the cavitation onset in our simulations, the full domain outlet pressure has been lowered progressively. However, to get an easier convergence, the outlet boundary condition has been kept with a relative pressure (with regard to reference pressure) to 0 Pa, and the reference pressure in the general settings has been lowered.

In this study we refer to the sigma coefficient instead of the Thoma number because we lack the data to compute the latter.

To simulate cavitation, good initial conditions are needed in order to be able to find the solution. For this reason, a case without the cavitation module activated has been solved for each level of pressure, then the multiphase module has been activated and it has been solved considering the previous result as initial condition.

To simulate cavitation, liquid water and vapour water at 25°C are considered in the entire domain. Meanwhile, only liquid water is imposed at the inlet boundary. The nucleation value for the Rayleigh-Plesset is fixed to  $2 \cdot 10^{-6}$  m, and the saturation pressure to 2500 Pa, keeping the rest of default parameters.

Moreover, the sensitive study of the empirical parameters included in ZGB model has been made, playing with his values with the main goal of increase the amount of vapour. The relations between the parameters of the CFX Ansys, and the variables of the equation 5.37 are:

- $F_{\text{condensation}}/E_{\text{evaporation}} = F$ .
- Nuclei volume fraction (NVF) =  $r_{\text{nuc}}$ .
- Mean Diameter =  $R_{\text{nuc}}$ .

From the equation 5.37 it can be easily deduced that to increase the amount of vapour the  $F_{\text{evaporation}}$  and the NVF have to be increased whereas the rest of parameters have to be decreased.

Where  $F_{\text{condensation}}$  is the F of the ZGB equation that describes the shifted mass of vapour to liquid.

## 7. Simulations without cavitation

### 7.1. Monitored parameters

The monitors are simulated values shown at each iteration. Any property of the fluid in some place of the computational domain or a computed parameter can be used. It helps to test if the fluid behaviour is correct and to know if the final solution is stable enough to consider it good.

#### 7.1.1. Static simulation

For the static runner, three monitor points have been defined which are the average pressure at the inlet and at the outlet boundaries, and the torque acting on one blade.

As it is shown in the next figure, the solution can be considered good since the monitored parameter have a value which is stable enough. Moreover, the relative average pressure on the outlet surface is practically 0 Pa, the imposed value.

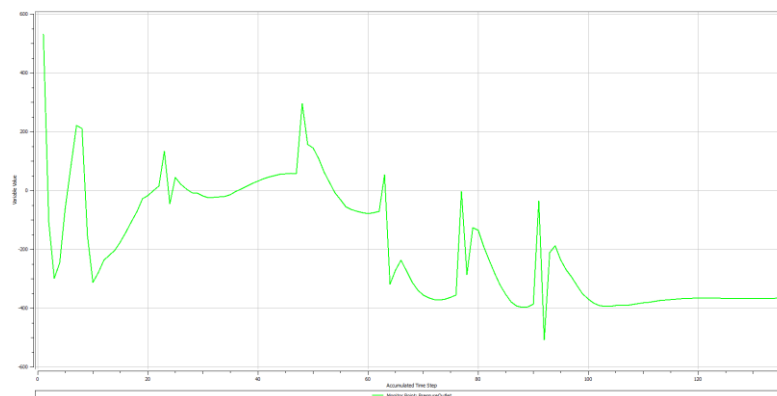


Figure 7.41: Outlet pressure

The torque obtained in this simulation is the 322 Nm, far from the experimental value indicated in section 6.1.2 which clearly indicates that this model is not good enough.

#### 7.1.2. Stage simulation

For the rotating runner, only two monitor points have been defined which are the pressure drop and the torque of one blade. In the next figure it can be seen the value of the torque for the model with a reference pressure of 1 atm.

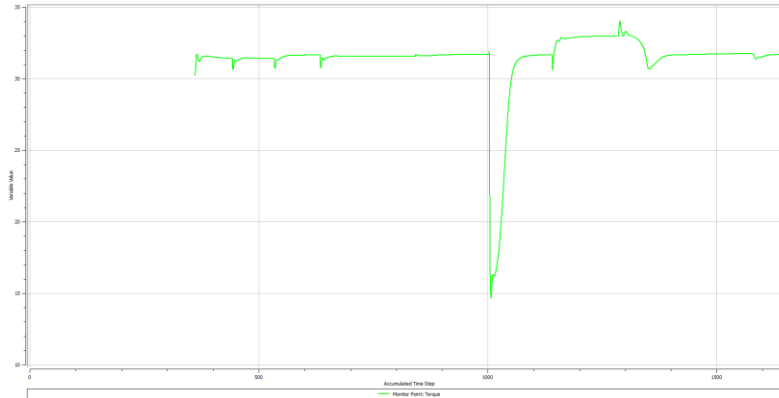


Figure 7.42: Torque

The torque obtained in this simulation is the 427,97 Nm. Comparing with the experimental value indicated in section 6.1.2, this result is similar to the expected one, verifying that the model is good. Moreover, the pressure drop has a similar behaviour to the torque when the sigma coefficient is lowered. This result is physically correct and can be considered a further evidence that the model is implemented correctly.

## 7.2. Analyse of the residues

When the complexity of the simulation increases to find the solution of the model is more difficult, increasing the time spent to converge. Thus, it is so important to have a good initial condition.

The solution is stopped if the RMS of the residues drops under  $1 \cdot 10^{-4}$  or if 1000 iterations have been done.

In some simulation, principally with the cavitation module active, two parameters of the solver control has had to be modified to get that the RMS residues drop under  $1 \cdot 10^{-4}$ . The Timescale Factor has had to be set to 0,25 and the convergence (an expert parameter) to 2.

In the next figure, where residuals corresponding to the three components of the velocity and the mass flow rate are plotted, it can be seen that the convergence is fast. However, when the cavitation module is turned on, the process is much longer.

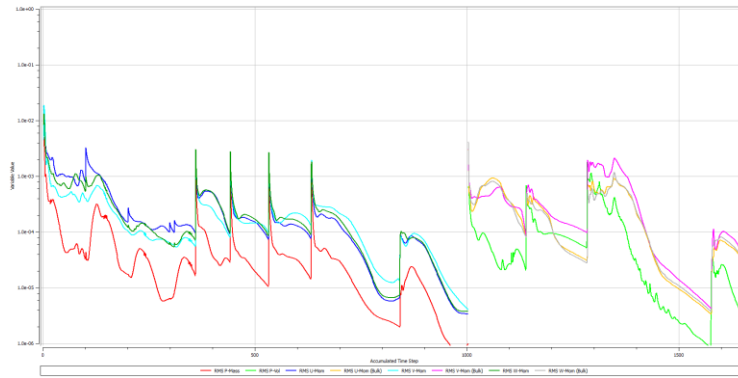


Figure 7.43: The residues

Other important values to check if the solution is good enough are the imbalances of the most important equations. In the next figure, the imbalances is shown, such as it can be seen the results are small enough.

Normalised Imbalance Summary		
Equation	Maximum Flow	Imbalance (%)
U-Mom	1.8640E+03	-0.0368
V-Mom	1.8640E+03	0.0031
W-Mom	1.8640E+03	-0.0222
P-Mass	2.8486E+02	0.0001

Figure 7.44: The imbalance study

### 7.3. Results of the simulations

The most realistic simulations for rotating machines should be obtained with a transient model, however, it requires a large computational capacity and a lot of time. Thus a steady-state method (stage) has become popular because requires less CPU memory and time, but the obtained results are less accurate.

The goal of these preliminary simulations is to learn how to simulate correctly rotating bodies and to get a good initial solution for the cavitation simulations. All simulations are done at BEP.

As already indicated, the work starts simulating a static turbine and imposing the relative velocity at the inlet boundary. Under such conditions, the behaviour of the fluid when it goes through the runner keeping the average pressure outlet to 1 atm has been studied.

The next step has consisted of carrying out a stage simulation. Likewise in the static simulation, firstly, the behaviour of the fluid into the runner setting the average pressure

outlet to 1 atm has been studied. Moreover, it has been tested that the two different cuts explained in section 6.2.1 give the same results.

### 7.3.1. Static simulation

The obtained results using K-epsilon and SST RANS models have been compared concluding that the results can change slightly between both. However, the SST model is more precise, thus it will be used for the following simulations.

In Fig. 7.45, a general view of the streamlines is shown. In general terms the flow velocities are low, thus it is expected that no cavitation should take place. On the other hand, that there is not boundary layer separation which confirms that the runner is working at BEP.

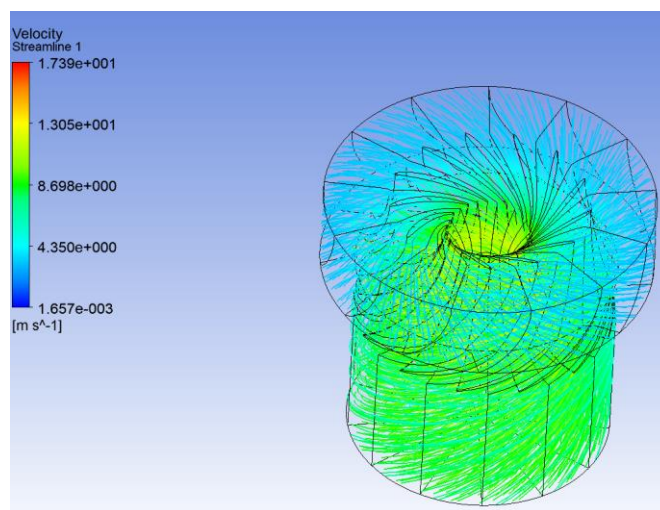


Figure 7.45: The stream line velocity

The inlet blade angle changes all the way from the top to the bottom along the leading edge. This is necessary to be well adapted to the incidence angle of the flow, which also changes because the inlet blade radius changes too. From the current results, it can be seen that the angle of attack is better at the top of the blade than at the bottom of the blade.

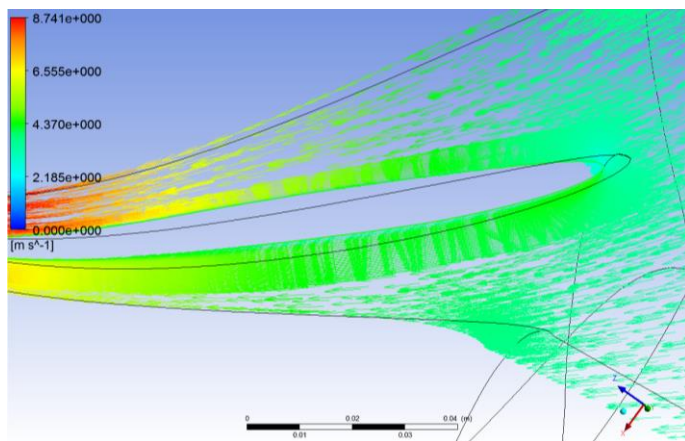


Figure 7.46: Attack angle at top blade

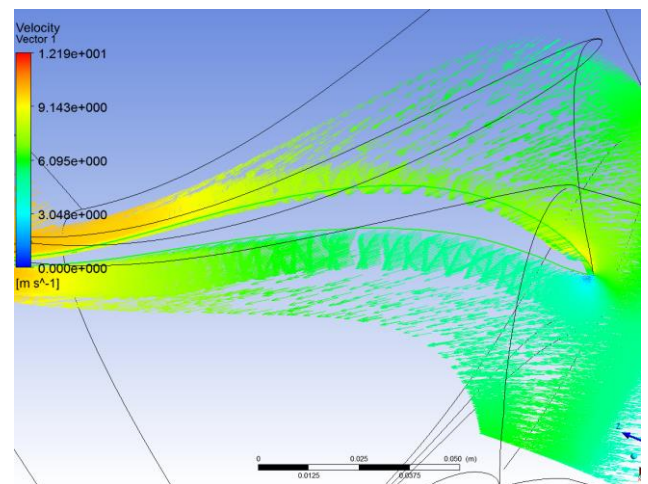


Figure 7.47: Attack angle at bottom blade

In the next figure, a large vortex can be seen at the bottom of the blade, where the velocity shows the worst angle of attack and there is some boundary layer separation.

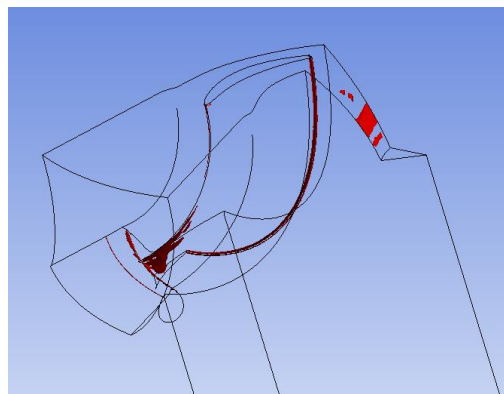


Figure 7.48: Vortex

There are two important magnitudes which are directly related with the torque. The pressure distribution on the blade and the force that makes the fluid on the blade due to the pressure.

Firstly, in the next two figures, the pressure distributions on each side of the blade can be seen. In the suction side, the pressure is lower than in the pressure side, according to the velocity values seen in figures 7.46 and 7.47. Knowing the direction of the runner's angular velocity these results are as expected.

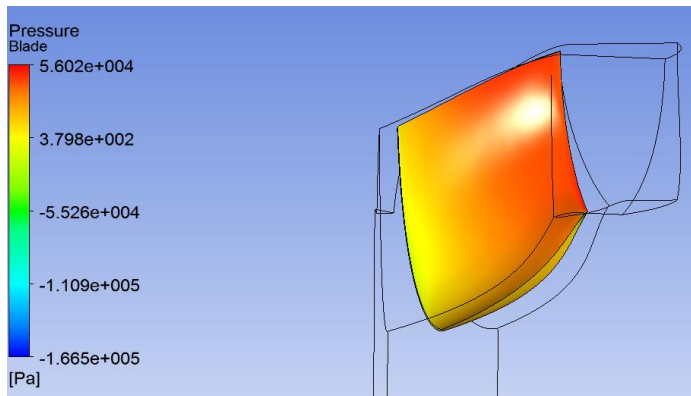


Figure 7.49: Pressure (pressure side)

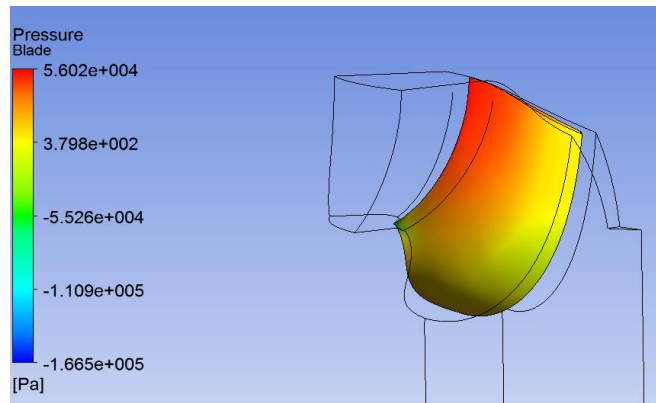


Figure 7.50: Pressure (suction side)

Similarly to the pressures, the results of force distribution are also as expected.

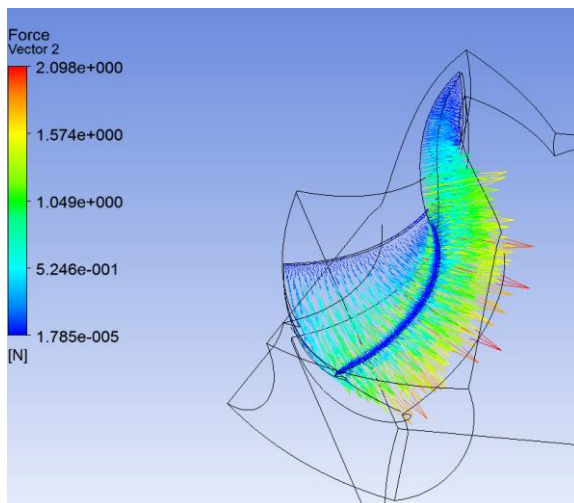


Figure 7.51: Force (pressure side)

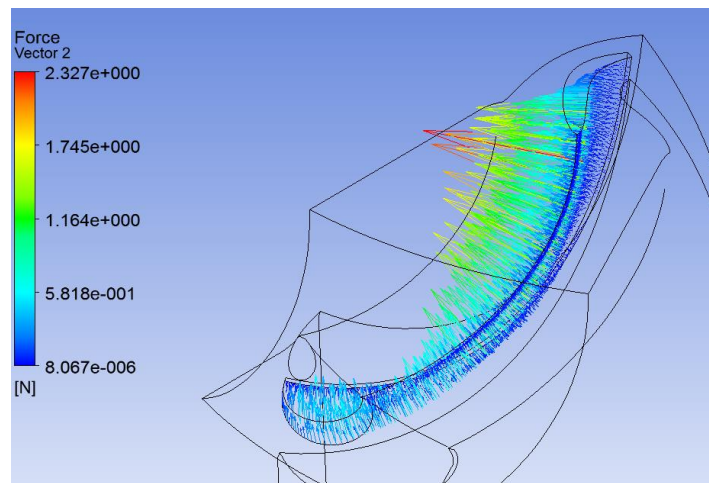


Figure 7.52: Force (suction side)

The total force in the suction side is lower than the total force in the pressure side. Thus, the torque has the same direction that the angular velocity of the runner.

Moreover, the highest values of force are at the farthest position from the rotational axis to maximize the total torque.

### 7.3.2. Stage simulation

In this section, the obtained results from a simulation imposing a reference pressure of 1 atm at the outlet section will be shown.

Like that in the static runner, the inlet blade angle is not in agreement with the flow angle of

attack from top to bottom. The coincidence is better at the top than at the bottom inlet of the blade as it can be seen in Fig. 7.53 and 7.54.

In the design of the runner blades the goal is to increase the efficiency and the power, and to avoid the cavitation [7]. For this reason, usually there is a trade-off, in order to satisfy these parameters, which provokes that in some slice of the blade a coarse angle of attack can appear. Consequently, cavitation can take place even at BEP and 100% efficiency cannot be achieved.

In next two figures, the flow angle of attack is not well aligned to the blade inlet.

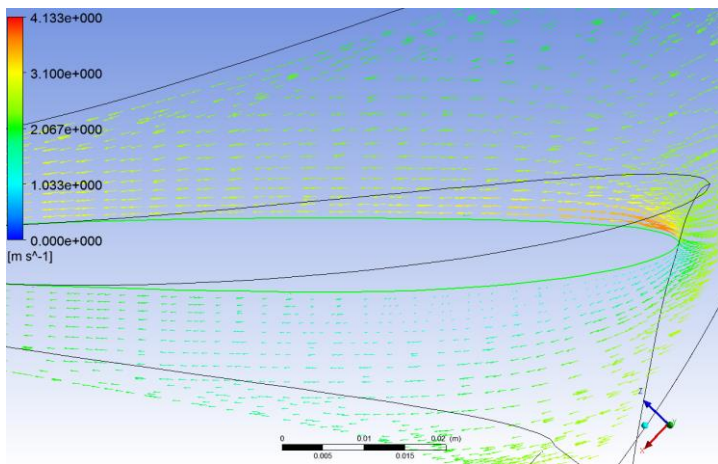


Figure 7.53: Attack angle at top blade

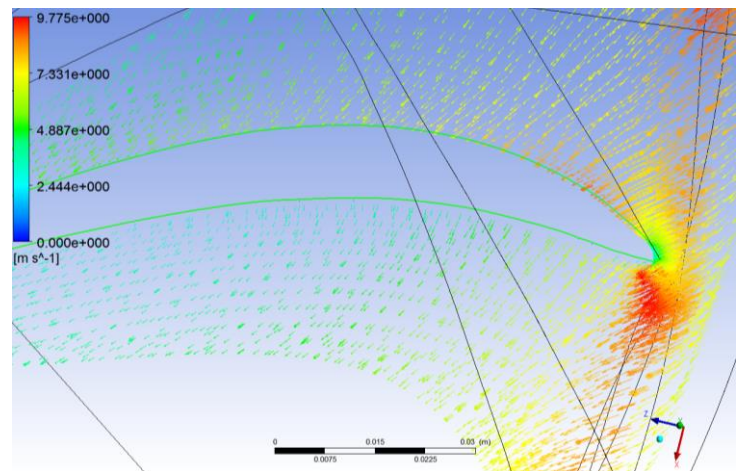


Figure 7.54: Attack angle at bottom blade

In the figure below, it is shown that some vorticity appears where the angle of attack is higher. However, the resulting vortexes are small allows which confirms that the turbine is working at BEP.

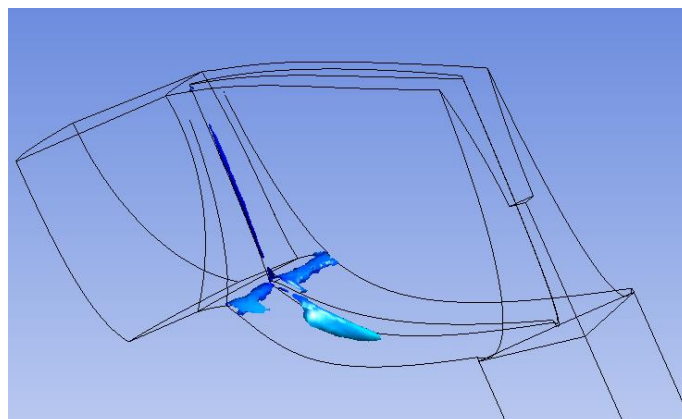


Figure 7.55: Vortex

In the next two figures (7.56 and 7.57), it is observed with the streamlines that there is no boundary layer separation.

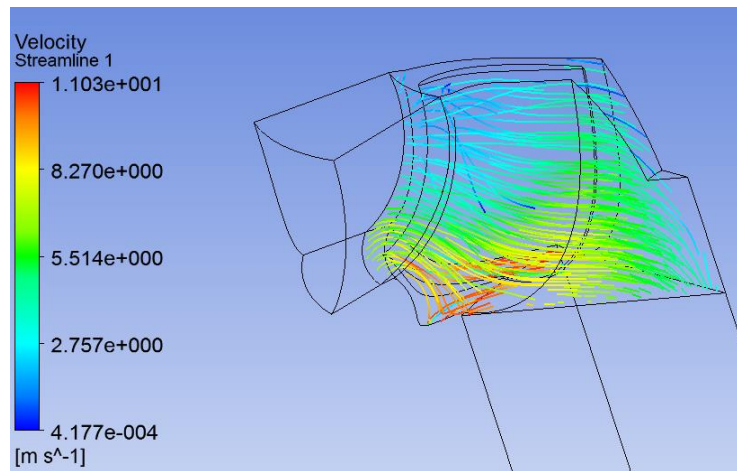


Figure 7.56: Streamline velocity in the runner

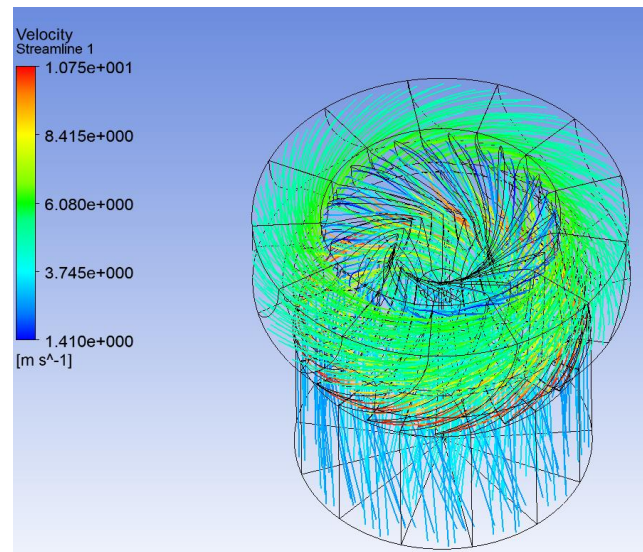


Figure 7.57: Streamline velocity

As observed in the figures below, the pressure is lower in the suction side and higher at the pressure side as expected.

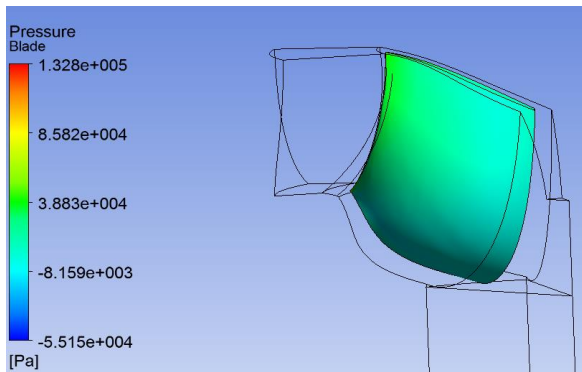


Figure 7.58: Pressure in suction side

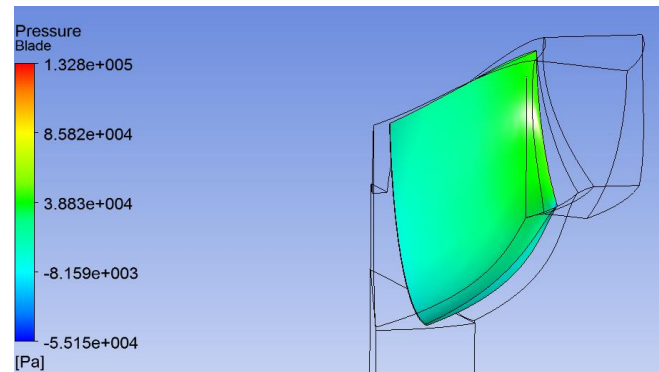


Figure 7.59: Pressure in pressure side

The distribution of forces is similar to the static turbine's case and it can also be seen that higher forces are generated at the beginning of the blade and they are significantly reduced at the end.

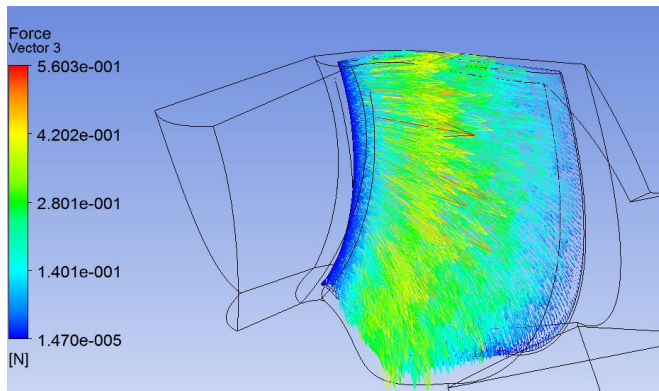


Figure 7.60: Force in pressure side

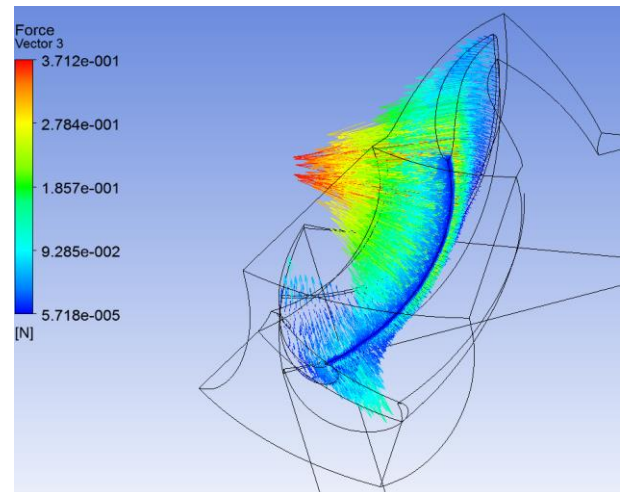


Figure 7.61: Force in suction side

## 8. Simulations under cavitation conditions

The cavitation that appears when the turbine is working at BEP by decreasing the sigma coefficient has been simulated. Each value of pressure has been associated with the corresponding value of the sigma coefficient. Attention has been given to when and where it appears and the consequences on the turbine's operation.

The procedure starts lowering the pressure at the outlet boundary until the saturation pressure of the water is achieved somewhere inside the fluid domain. Then, the cavitation model is activated.

### 8.1. Vapour volume fraction

In the next figures, the vapour volume fraction ( $\alpha$ ) is plotted on the suction side of the blade. The higher the value, the larger amount of cavitation is expected due to bubbles or cavities. The blue colour indicates that there is not any fraction of vapour so the fluid is totally liquid ( $\alpha = 0$ ). However, if there is some vapour, the colour will become red. When all the fluid in the element is vapour  $\alpha$  will become 1.

It is observed some local vapour at the inlet of the blade. In fact, the blade design is not perfect because there is a trade-off between the fabrication cost, the efficiency of the turbine and the onset of cavitation. This type of cavitation is explained in section 5.2 and it is not sensitive of the sigma value, it is more influenced by the blade geometry and the flow incidence angle. For this reason this type of cavitation will appear in all simulations in the same way.

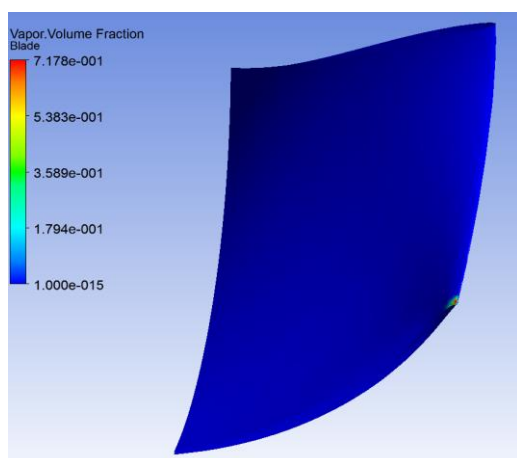


Figure 8.62: First type of cavitation

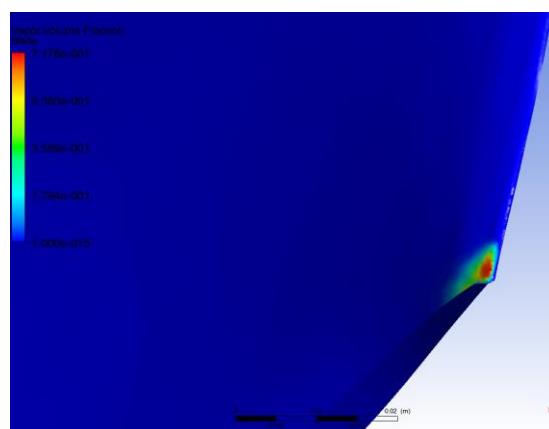


Figure 8.63: First type of cavitation (zoom)

In the next figures, another type of cavitation is observed as sigma is decreased.

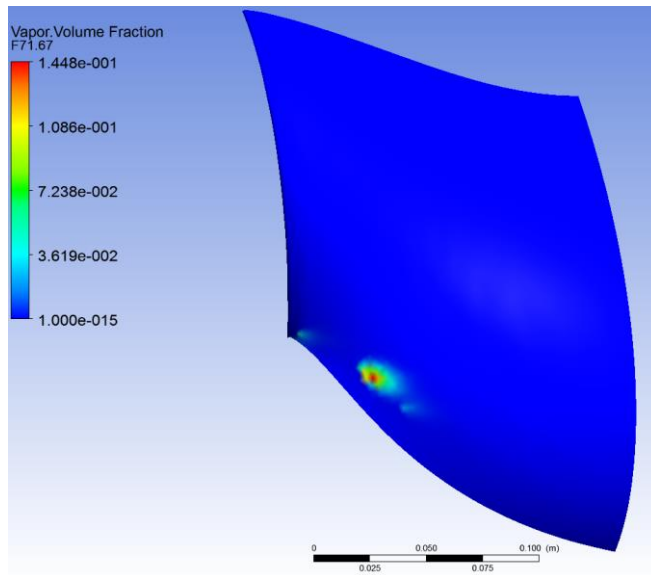


Figure 8.64:  $\sigma = 1,24$

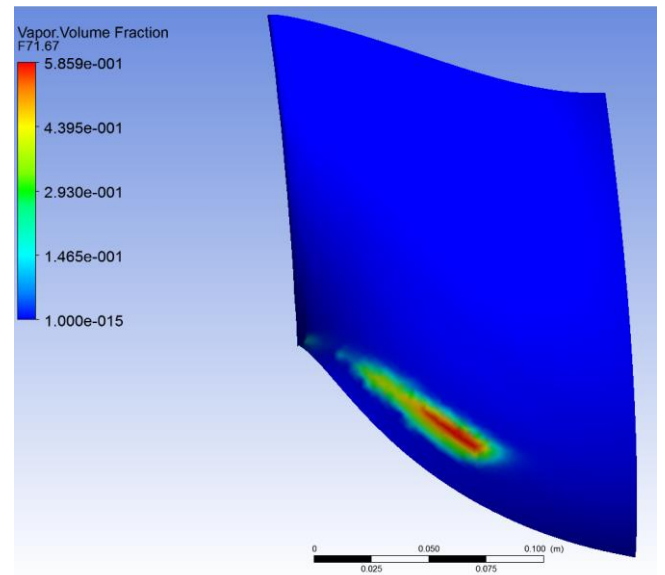


Figure 8.65:  $\sigma = 0,99$

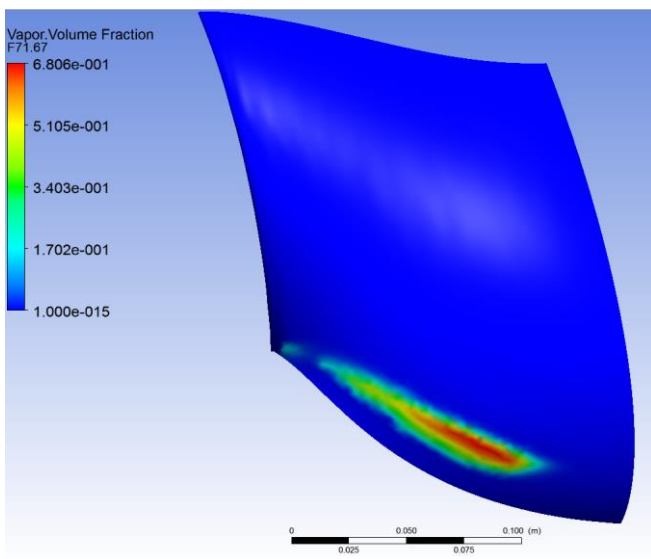


Figure 8.66:  $\sigma = 0,84$

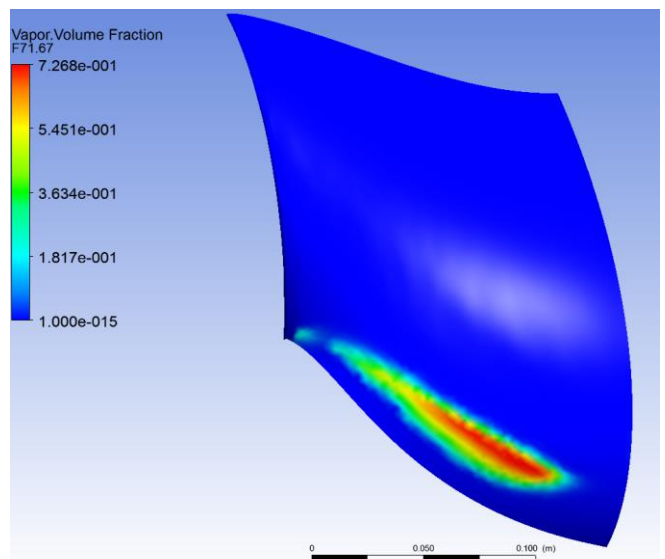


Figure 8.67:  $\sigma = 0,74$

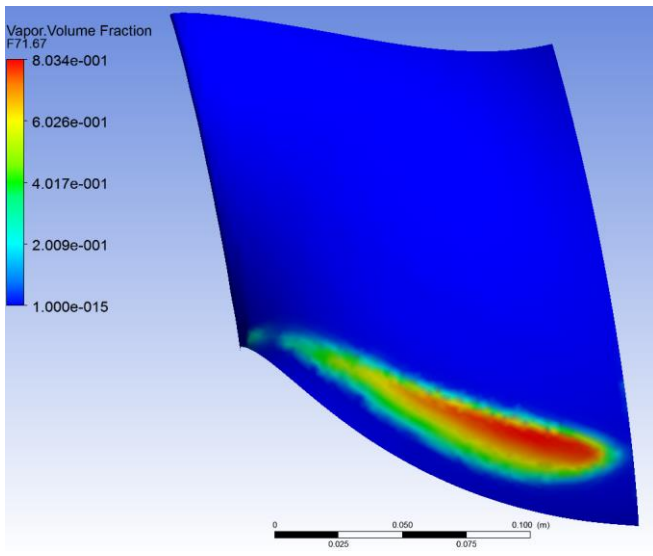


Figure 8.68:  $\sigma = 0,59$

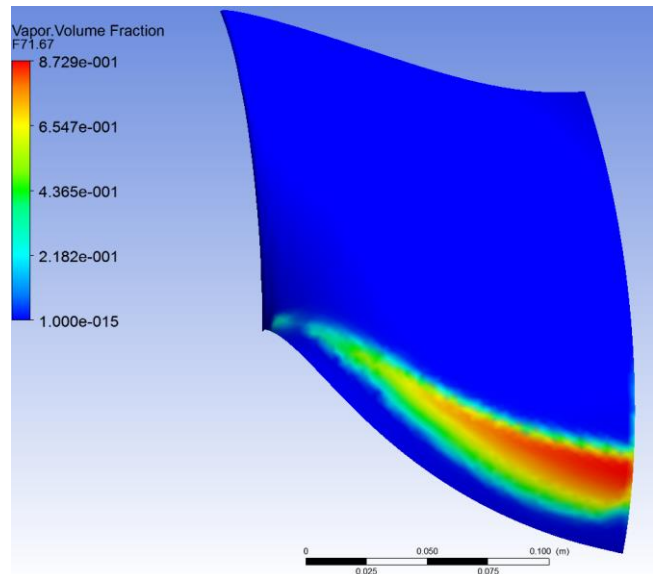


Figure 8.69:  $\sigma = 0,49$

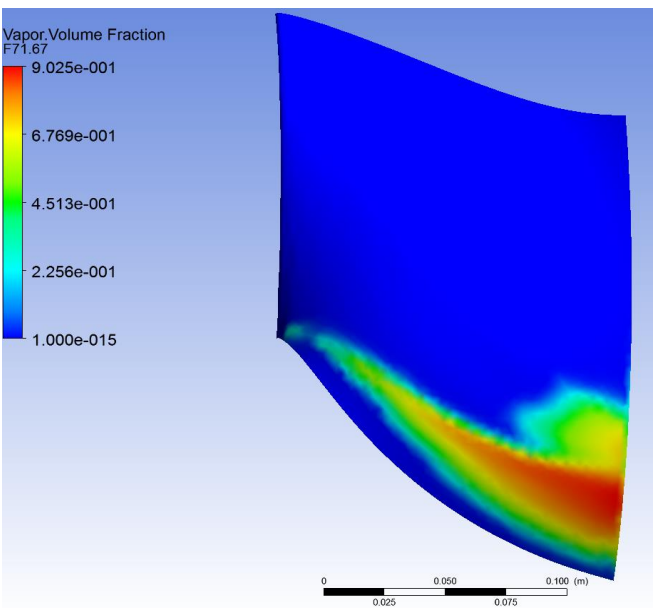


Figure 8.70:  $\sigma = 0,35$

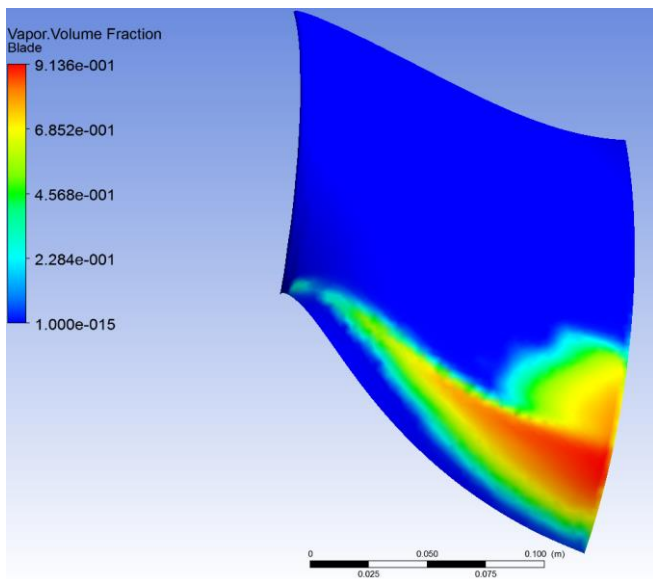


Figure 8.71:  $\sigma = 0,25$

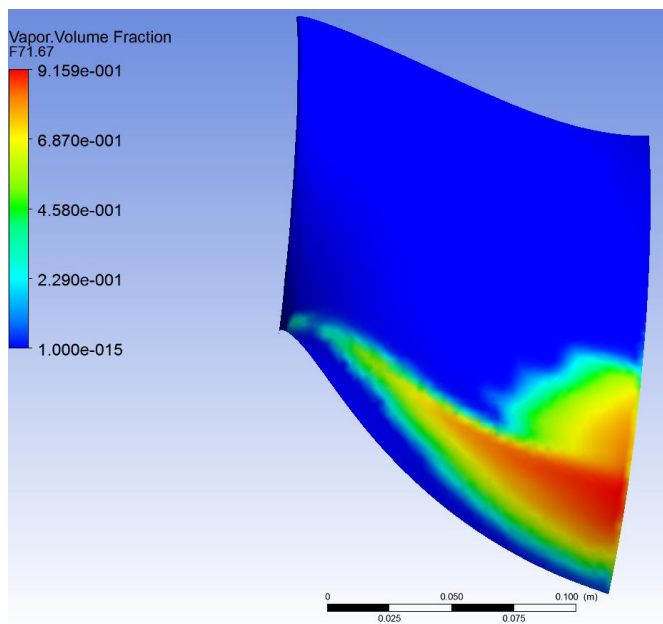


Figure 8.72:  $\sigma = 0,15$

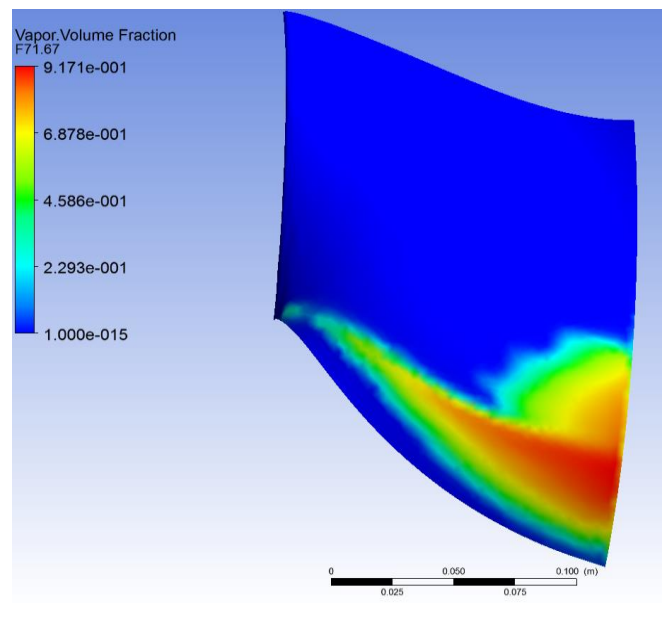


Figure 8.73:  $\sigma = 0,05$

The position of the cavity and its onset pressure is very similar to the results in [10-11]. This agreement confirms that the model used in these simulations is good enough.

It can be seen that cavitation starts when the outlet pressure is 12500 Pa and the sigma coefficient is 0,99. A cavitation sheet is only considered if the 50 per cent of the fluid in this area is in vapour state.

On the other hand, it can be claimed that due to the good design of the turbine, the dimensions of the GAMM Francis turbine and the computational domain, a big sheet of vapour which covers the entire suction face of the blade provoking the fall of the torque have not been obtained for any sigma simulated. The maximum amount of vapour that can be obtained corresponds to a sigma of 0,05 for an outlet pressure of 3000 Pa, practically the vapour pressure.

These results can be considered correct based on the fact that the studied point is the BEP where the highest efficiency and the greatest resistance of the cavitation are supposed.

## 8.2. Area covered by cavitation

To understand better the cavitation behaviour, the area of the blade with cavitation has been calculated and related to sigma. Any area with a vapour volume fraction equal or higher than 0,5 has been considered as developed cavitation.

In the next table, it is clear how the area of the cavitation increases when the sigma value is lowered.

$\sigma$	Area (cm <sup>2</sup> )	Area (% of blade)
9,79	0	0
1,24	0	0
0,99	1,36	0,44
0,84	4,08	1,32
0,74	7,23	2,34
0,59	13,12	4,24
0,49	19,7	6,37
0,35	30,79	9,96
0,25	38,13	12,33
0,15	40,02	12,94
0,05	40,96	13,24

*Table 8.1: Area covered by cavitation*

In the next figure, the evolution of the cavitation shape and area is shown.

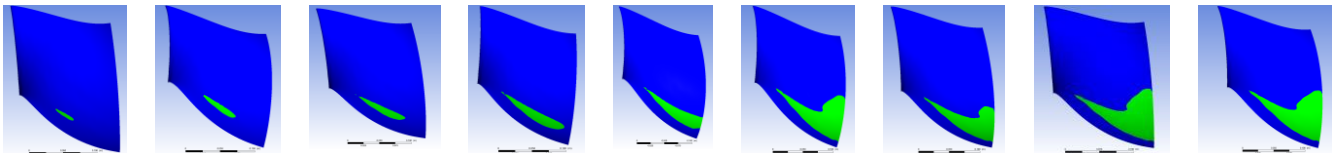


*Figure 8.74: Area's evolution*

It has been proven that for a certain value of sigma number the amount of vapour grows very quickly, however this fact cannot be observed in the figure 8.75 since this value has not been able to be got.

In the next graph, it is shown how the percentage of sheet cavitation area relative to total suction side area increases when the sigma drops. The fastest growth is observed from sigma 1 to 0,1.

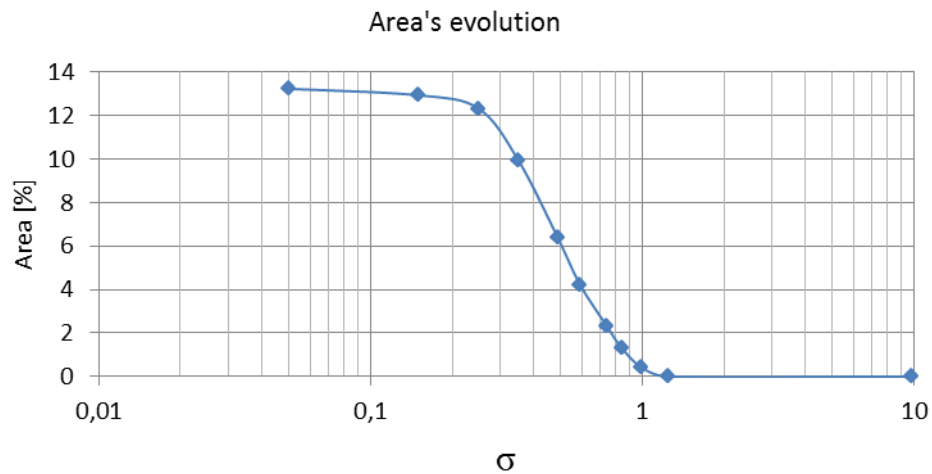


Figure 8.75: Area's evolution

The fact that the vapour doesn't cover the entire suction side area although a very low sigma is imposed is due to the short draft tube simulated in our model. The outlet boundary should be located further downstream than the runner so that a lower pressure could be achieved on the blades.

To find more cavitation, according to the theory explained in the section 5.1, we could have tried to simulate another operation point more critical for cavitation. For example, an operation point with a higher discharge.

### 8.3. Torque

To determine the torque a CFX function has been used. In the next table the values of the torque and their change respect to the torque without cavitation are indicated for each sigma.

$\sigma$	Torque (Nm)	% of change
9,79	31,69	0
1,24	31,69	0
0,99	31,76	0,22
0,84	32,05	1,15
0,74	32,24	1,76
0,59	32,60	2,89
0,49	32,88	3,76
0,35	32,99	4,13

0,25	32,96	4,01
0,15	32,89	3,83
0,05	32,73	3,29

Table 8.2: Torque

The next graph plots the evolution of the torque in relation to the sigma. It can be observed that the torque is constant until the onset of cavitation and then it starts to increase. Then, for sigma equal or lower than 0,35 the torque drops although the expected total drop cannot be seen due to the current limitations of our model and the operation at BEP.

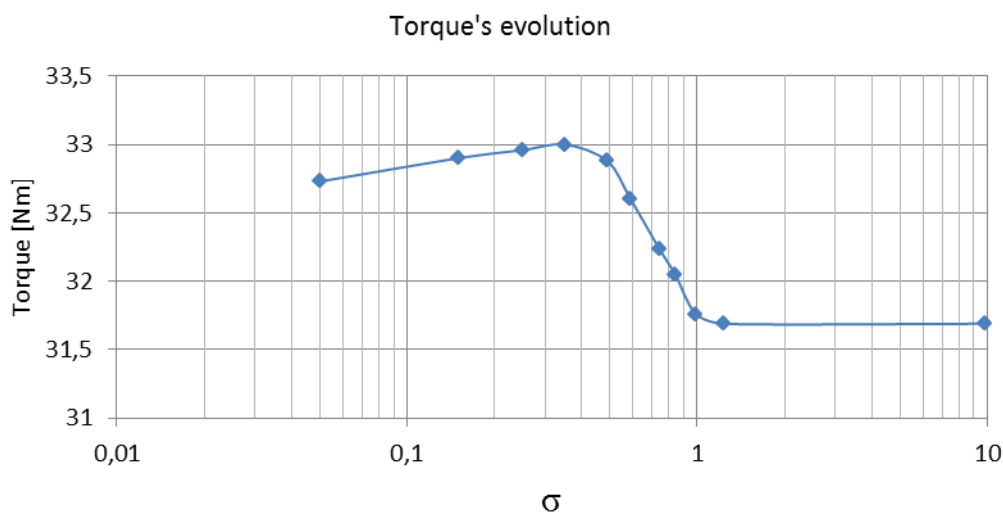


Figure 8.76: Torque

## 8.4. Pressure coefficient

Two different representations of pressure coefficients,  $C_p$ , for each sigma number are shown. On the one hand, the  $C_p$  has been plotted on the blade surface. On the other hand, they are plotted along a line traced along the more relevant direction. The selected line has been selected differently for each sigma since the cavity moves. The horizontal axis refers to the distance from the axis coordinates.

To calculate the  $C_p$ ,  $P_{ref}$  is the pressure set at the outlet boundary that changes for each sigma number,  $V_{ref} = W$  is 4,49 m/s and  $\rho$  is 997,78 Kg/m<sup>3</sup>.

The areas where  $C_p$  is lower or equal to  $-\sigma$  the cavitation will onset. From figure 8.76, it can be assumed that cavitation appears when the sigma is 0,99. Next table shows the sigma

value for each  $P_{ref}$ .

$P_{ref}$ (Pa)	$\sigma$
101325	9,79
15000	1,24
12500	0,99
11000	0,84
10000	0,74
8500	0,59
7500	0,49
6000	0,35
5000	0,25
4000	0,15
3000	0,05

Table 8.3: Pressure of reference

Here below, two figures with  $C_p$  values can be seen, one for the suction side and the other for the pressure side for each sigma. The blue colour indicates the areas of the blade with a  $C_p$  equal to the  $-\sigma$  where vapour must be present.

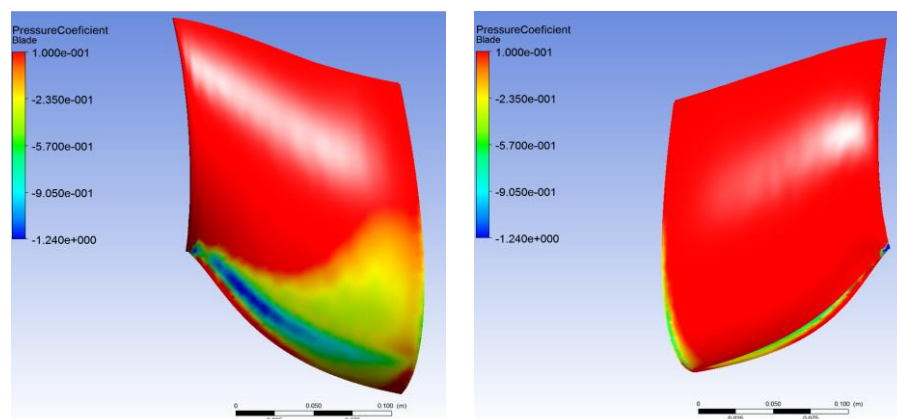


Figure 8.77:  $\sigma = 1,24$

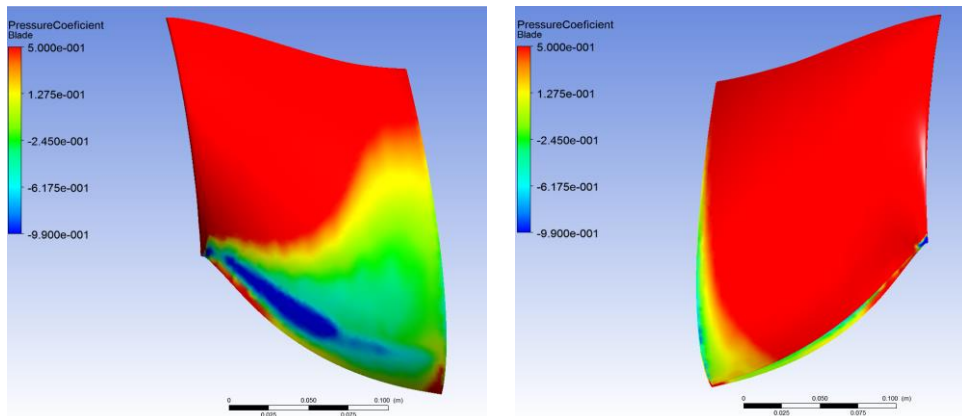


Figure 8.78:  $\sigma = 0,99$

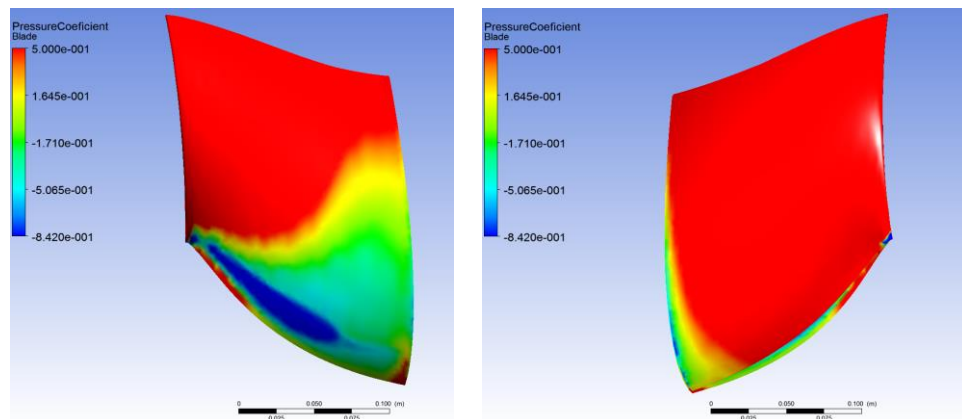


Figure 8.79:  $\sigma = 0,84$

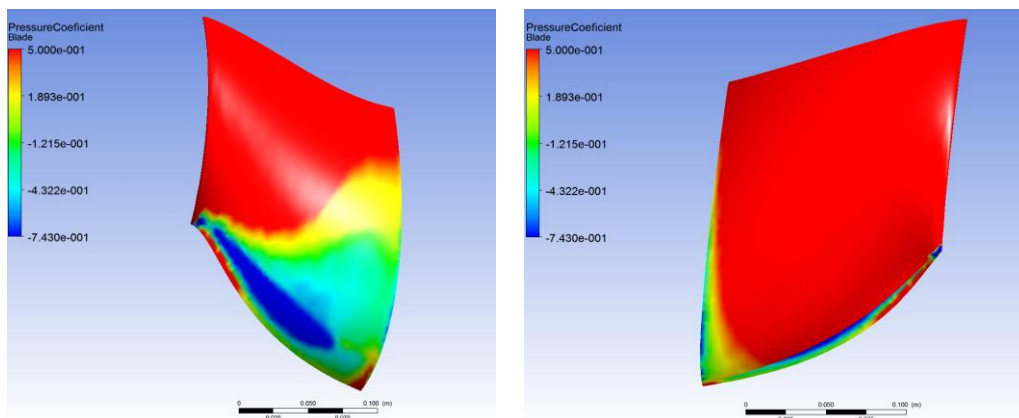


Figure 8.80:  $\sigma = 0,74$

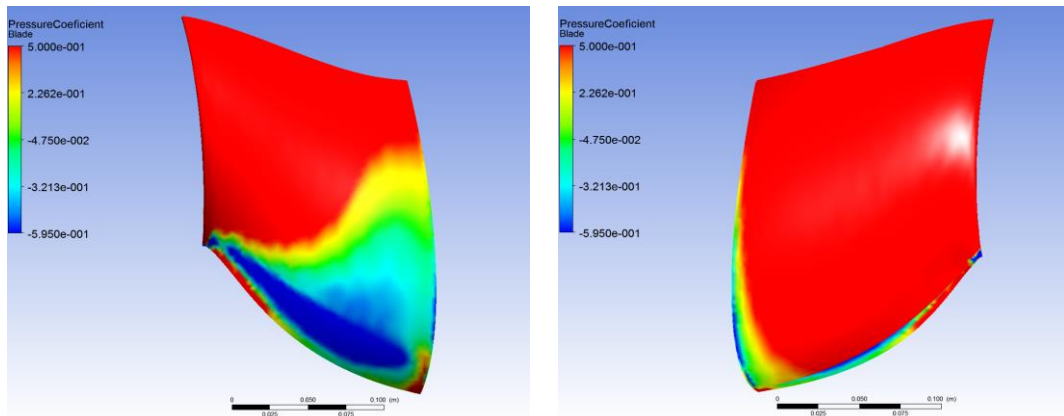


Figure 8.81:  $\sigma = 0,54$

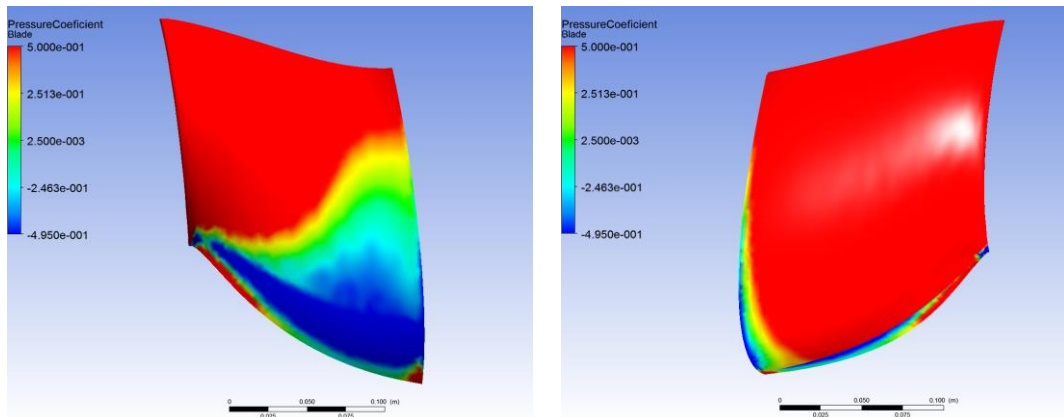


Figure 8.82:  $\sigma = 0,49$

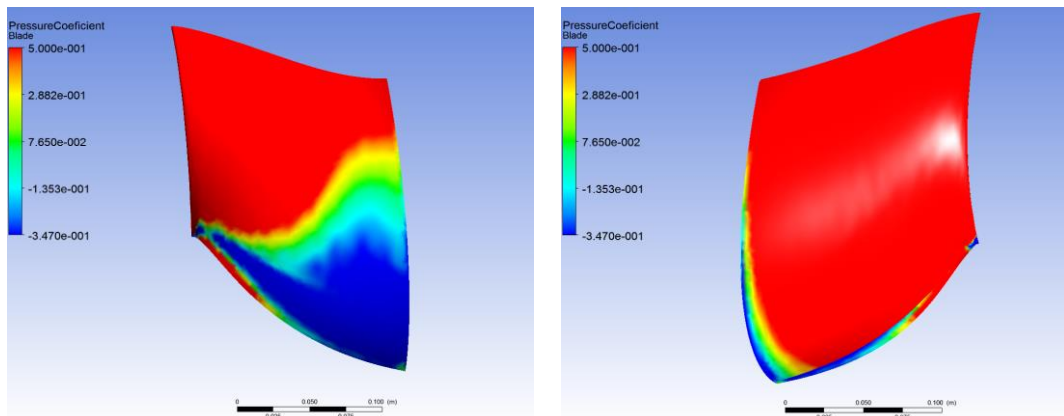


Figure 8.83:  $\sigma = 0,35$

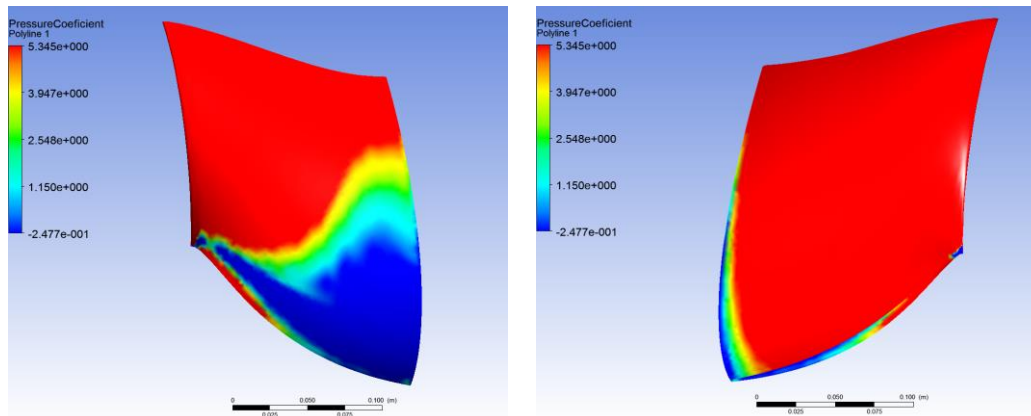


Figure 8.84:  $\sigma = 0,25$

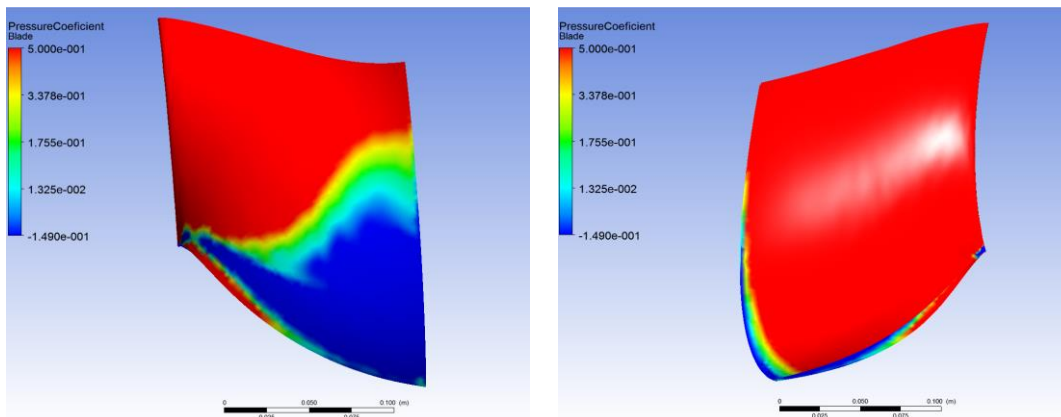


Figure 8.85:  $\sigma = 0,15$

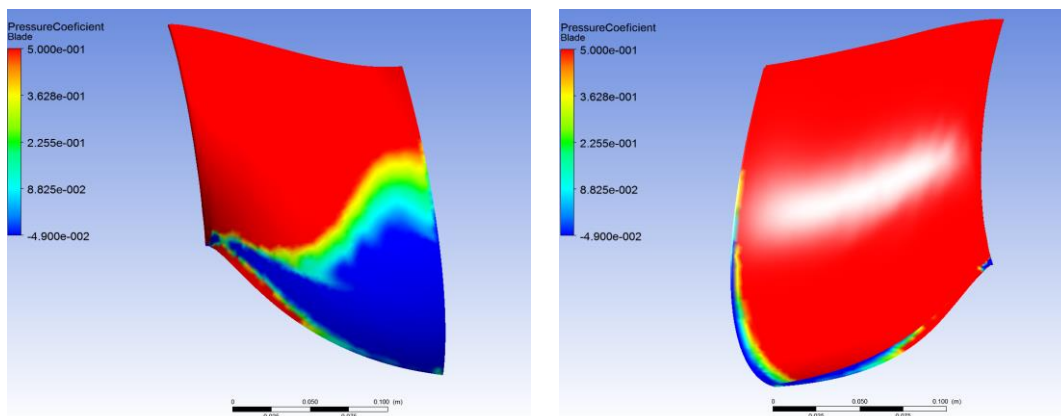


Figure 8.86:  $\sigma = 0,05$

On the pressure side, the area with  $C_p = -\sigma$  is always the same independently of the outlet pressure imposed, because this type of cavitation is not sensitive to  $\sigma$ . However, on the suction side, the area with a pressure coefficient changes significantly according to the

sigma.

Moreover, according to the ZGB cavitation model equations, when the condition  $C_p = -\sigma$  is achieved some amount of vapour is generated. However, it is possible that the fraction of vapour is very little. By changing the empirical parameters of the model, this fraction of vapour could change.

For the lowest sigma, the pressure coefficient plotted in the edge suction and pressure side is shown in the next figure.

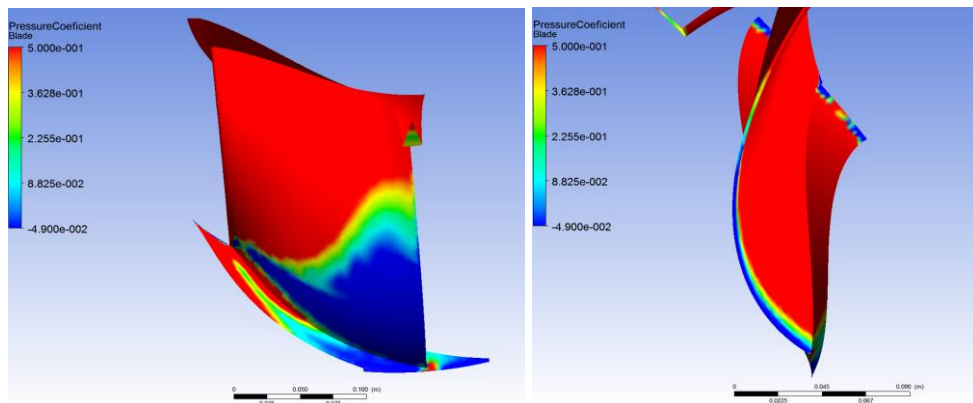


Figure 8.87:  $\sigma = 0,05$

In the next graphs, the evolution of the pressure coefficient along a line crossing the cavitation area is shown for all the sigma values.

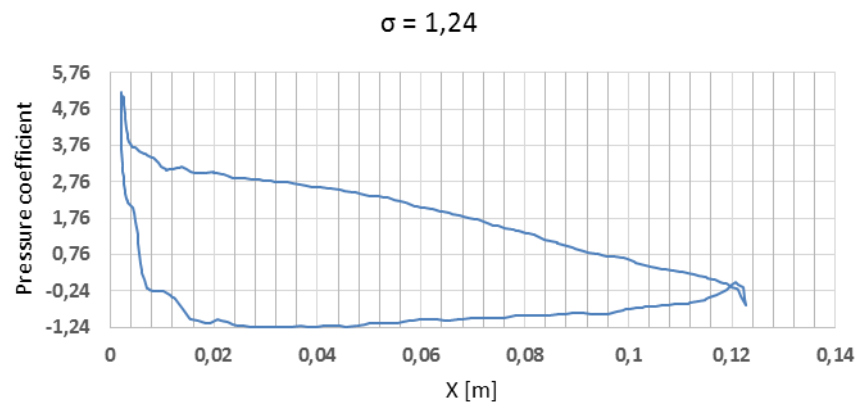


Figure 8.88

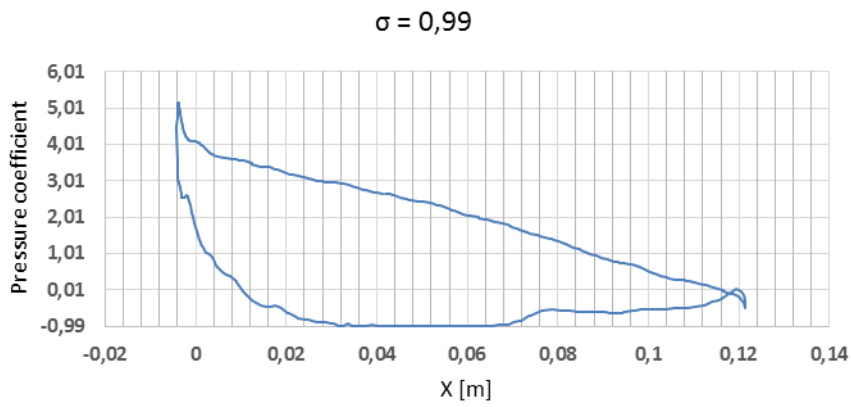


Figure 8.89

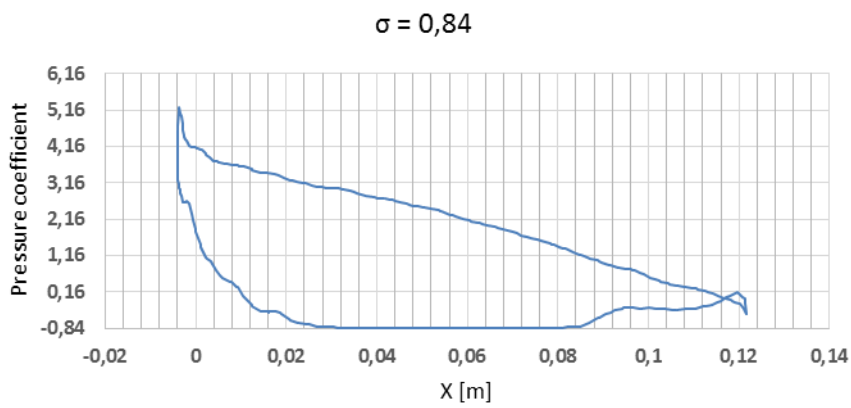


Figure 8.90

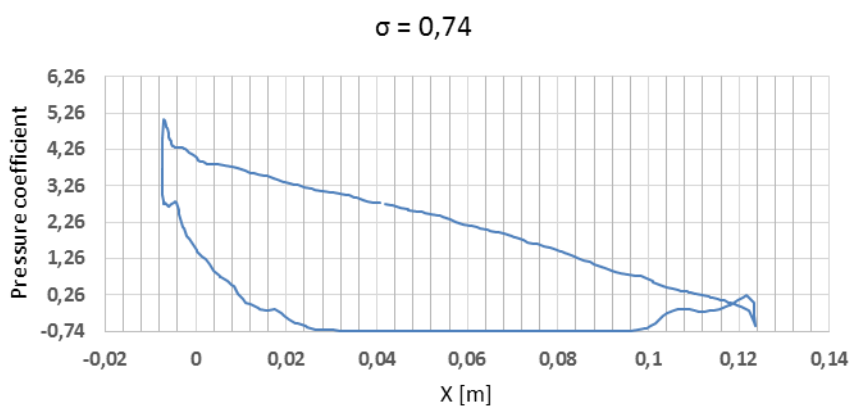


Figure 8.91

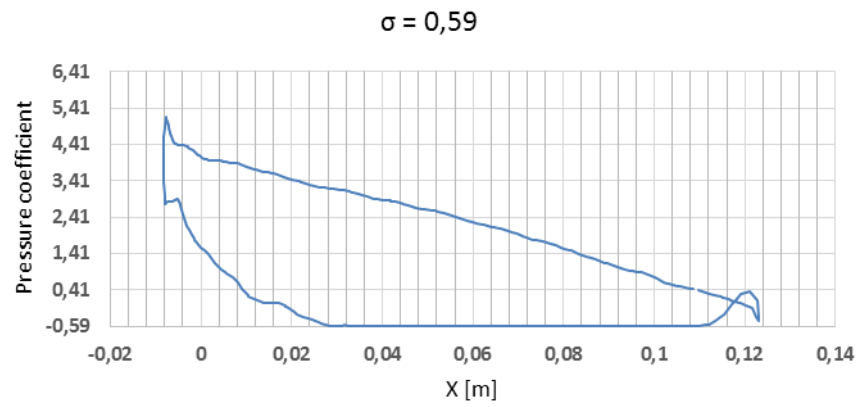


Figure 8.92

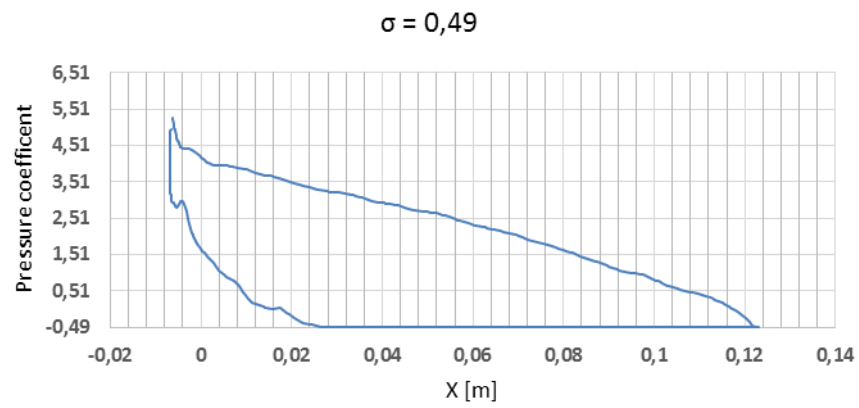


Figure 8.93

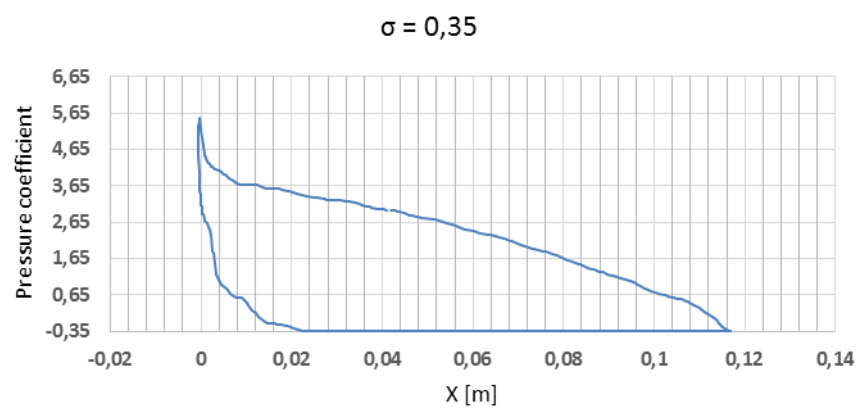


Figure 8.94

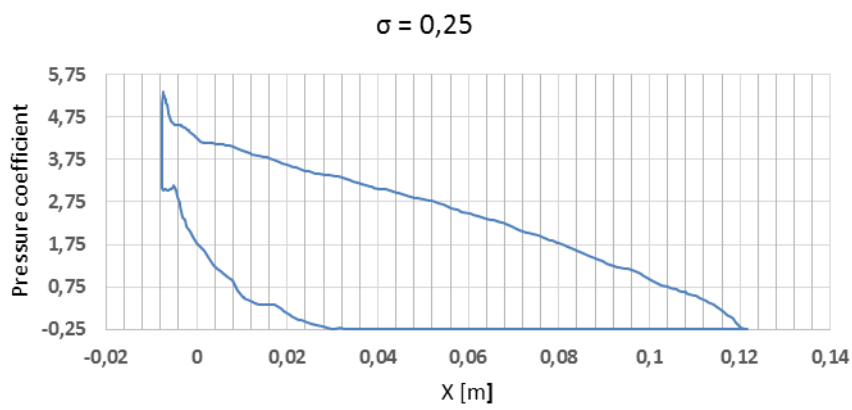


Figure 8.95

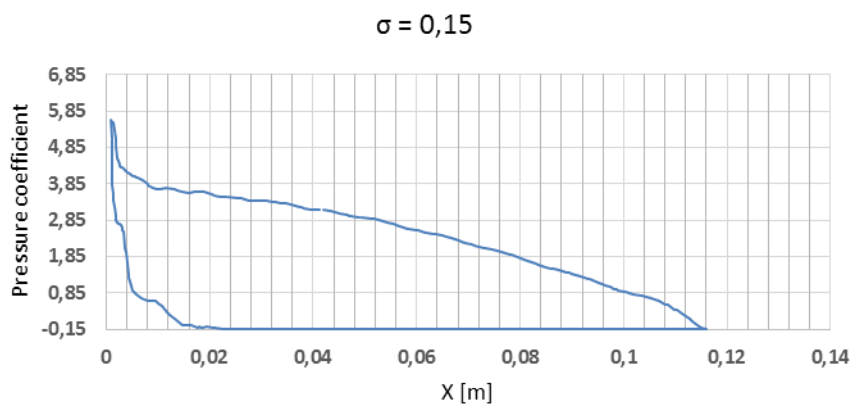


Figure 8.96

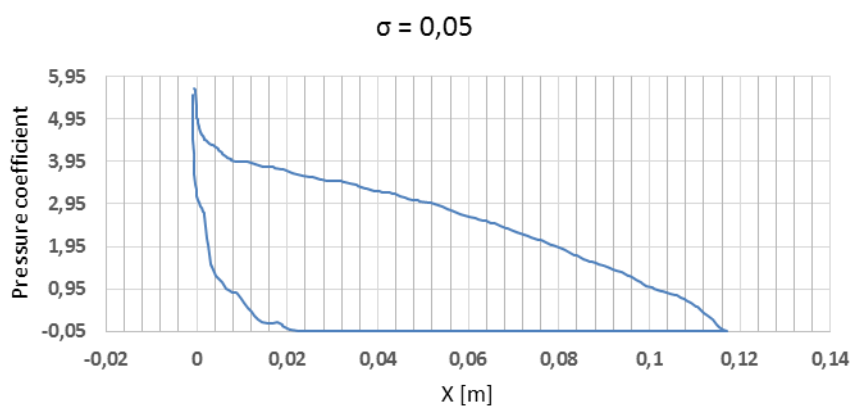


Figure 8.97

## 8.5. Head

The head has been determined between the inlet and outlet surfaces of the runner.

Firstly, the velocity in outlet surface will be studied. As shown in the next graph, the velocity increases when the sigma decreases because the effective outlet section is reduced by the presence of a cavitation swirl.

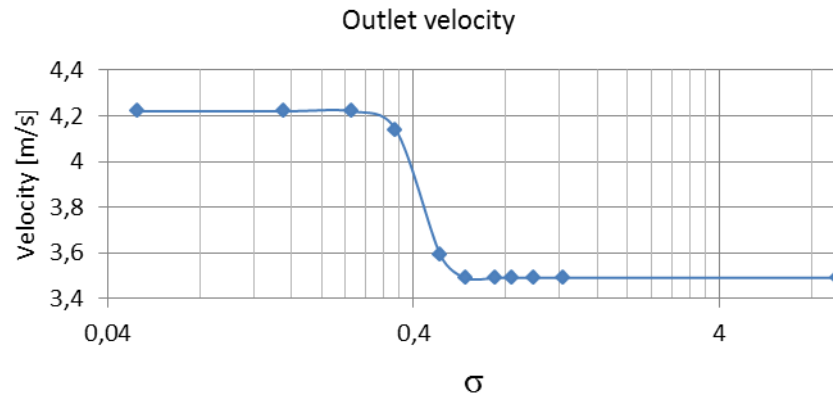


Figure 8.98

Since the inlet velocity is constant, the dynamic pressure decreases when sigma is decreased as it can be seen in the next graph.

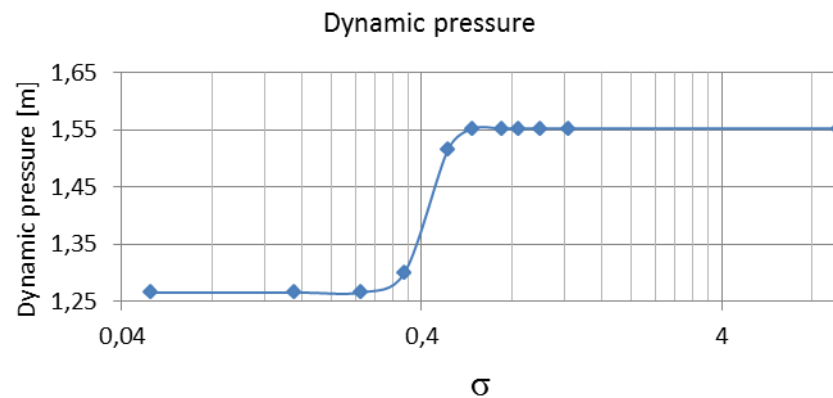


Figure 8.99

However, the static pressure shows a growing trend like it is shown in the next graph.

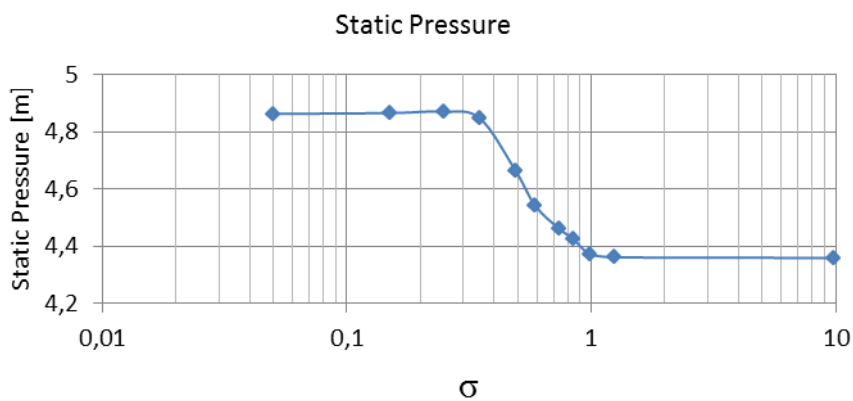


Figure 8.100

According to the head equation, the total pressure behaviour will be exactly the same as the one of the head coefficient. For this reason, only the head coefficient graph will be shown.

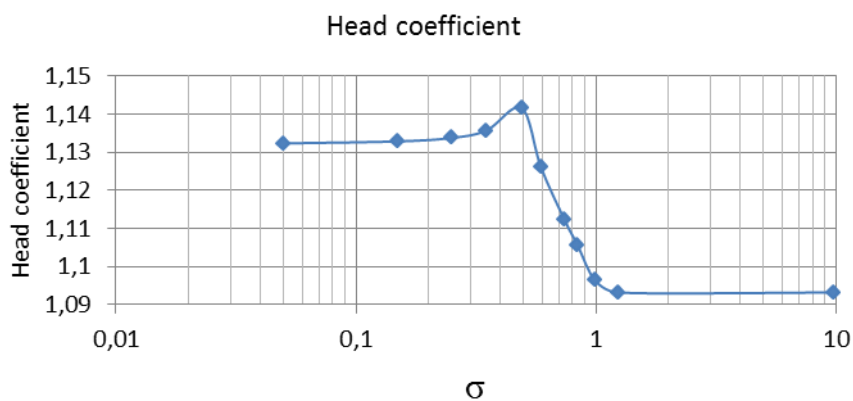


Figure 8.101

As it can be seen in the above graph, the expected behaviour and trend of the torque is well simulated although the final shut down is not obtained.

## 8.6. Sensitivity analysis of the cavitation model

The impact of different empirical parameters of the cavitation model on the position, shape, amount of vapour and thickness of the cavitation as well as the resulting torque has been analysed. The simulation results and the default parameters for an outlet pressure of 3000 Pa have been taken as a reference to see the effects of changing them one by one while keeping the rest constant. In the next table, the default values and the new values taken for

each parameter are listed.

Empiric parameter	Default value	Set value
$F_{\text{condensation}}$	0,01	0,00001
$F_{\text{evaporation}}$	50	50000
Nuclei Volum Fraction (+)	$5 \cdot 10^{-4}$	0,5
Mean Diameter	$2 \cdot 10^{-6}$ m	$2 \cdot 10^{-8}$ m
Nuclei Volum Fraction (-)	$5 \cdot 10^{-4}$	$5 \cdot 10^{-6}$

Table 8.4

In the next figures, the reference vapour volume fraction is shown on the left of each one, and the picture with the new results changing the corresponding parameter are shown on the right.

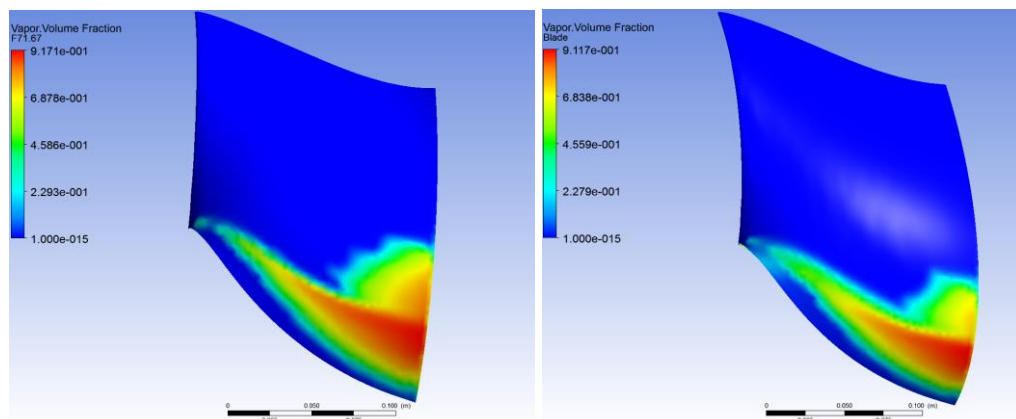


Figure 8.102:  $F_{\text{condensation}}$

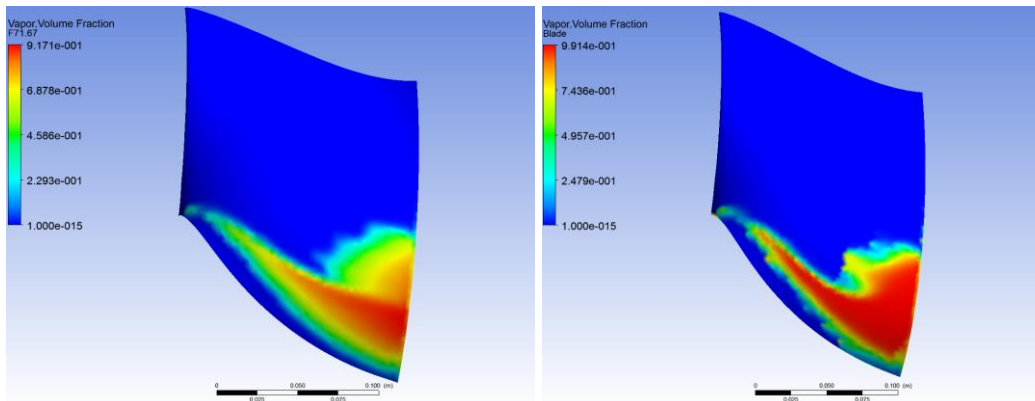


Figure 8.103: Fevaporation

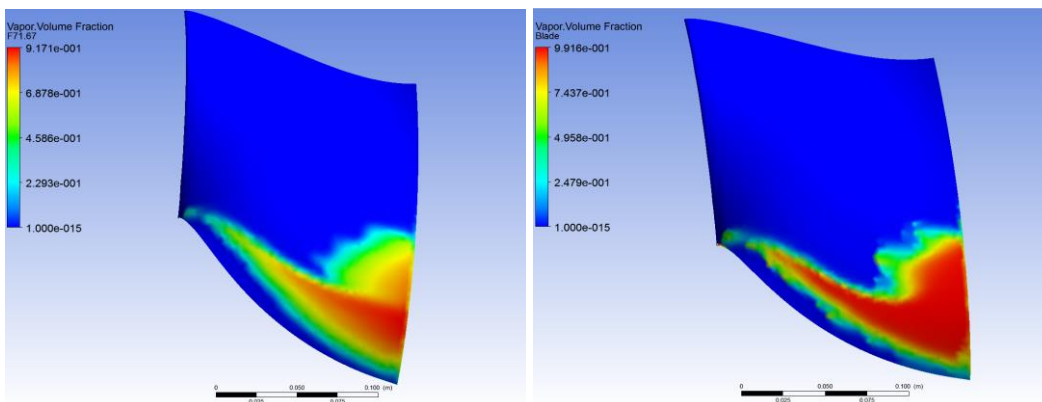


Figure 8.104: NVF(+)

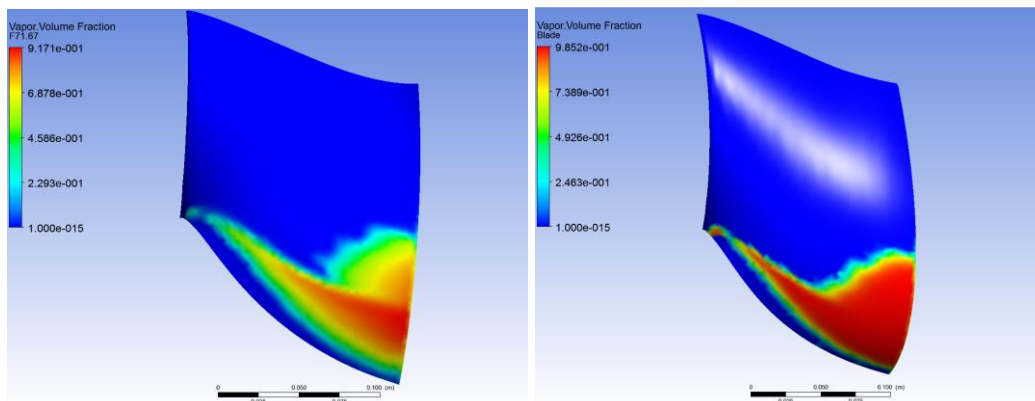


Figure 8.105: Mean diameter

The  $F_{\text{condensation}}$  practically does not change the results obtained because this parameter is applied in the regions where the vapour is shifted to liquid. In the current results, the condensation takes place downstream the runner blades far inside the draft tube. On the contrary, all the rest of parameters increase the vapour amount being the Mean Diameter

the parameter with greater impact.

The position of the cavity remains unchanged in any simulation and the shape only changes slightly at the edge of the cavity when changing the  $F_{\text{evaporation}}$  and the Nuclei Volume Fraction, where it becomes more irregular.

In the following figures, the thickness of the cavity is shown with an isosurface for the vapour volume fraction of 0,5. On the left, the results corresponding to the default values are shown, and on the right, the results when one parameter is changed are shown.

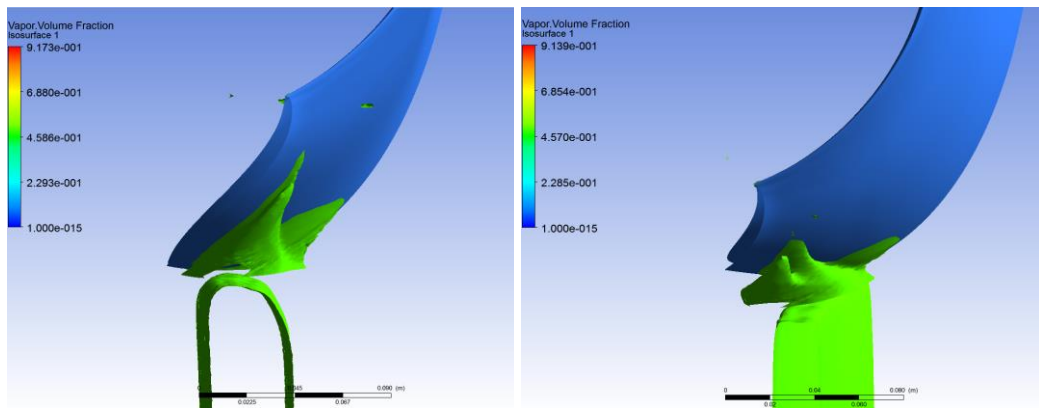


Figure 8.106:  $F_{\text{condensation}}$

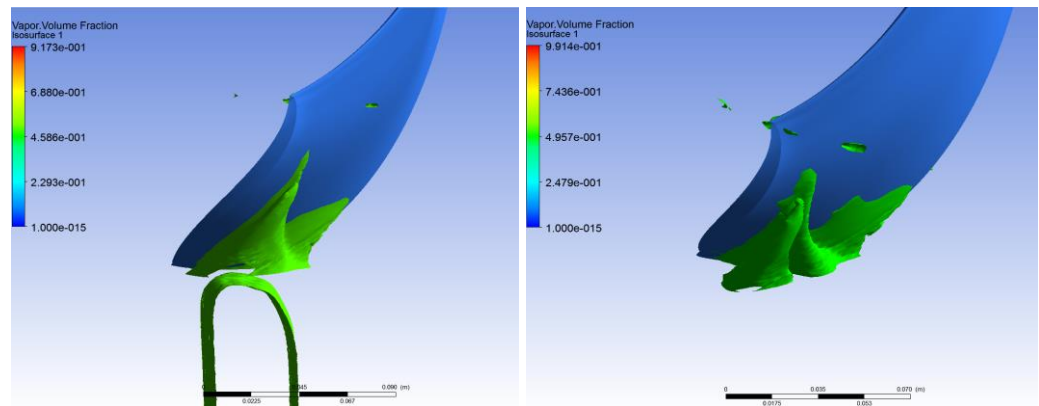


Figure 8.107:  $F_{\text{evaporation}}$

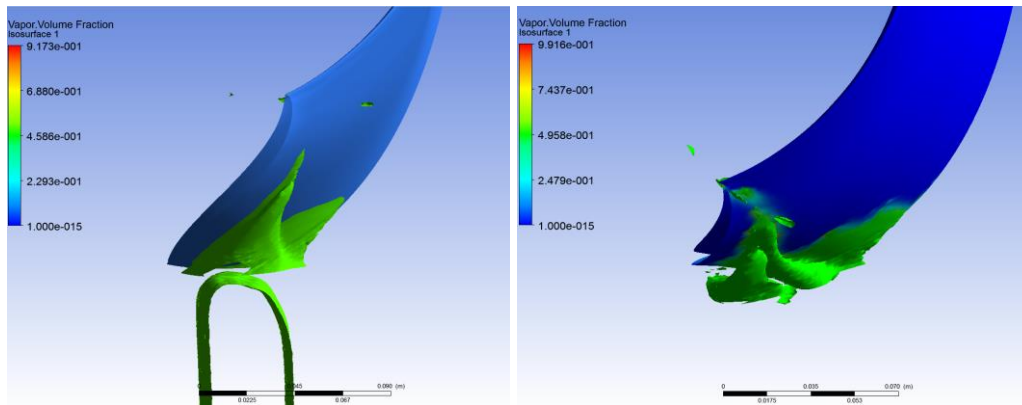


Figure 8.108: NVF(+)

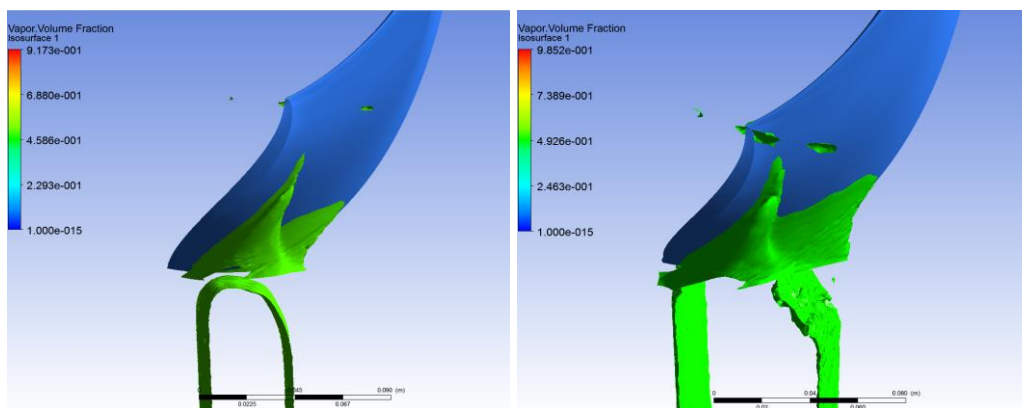


Figure 8.109: Mean diameter

In all the cases, the thickness increases slightly except when the  $F_{\text{condensation}}$  is changed. In this case, it remains practically constant. On the other hand, it is shown how with  $F_{\text{evaporation}}$  and Nuclei Volume fraction changes the vapour under the blade disappears.

Another view of the thickness' change according the value of the empirical parameters is shown in the next figures where the vapour volume fraction is plotted on a horizontal plane cutting the blade. The left figures show the obtained results with a default value and the right pictures show the results of the simulations where one parameter is modified.

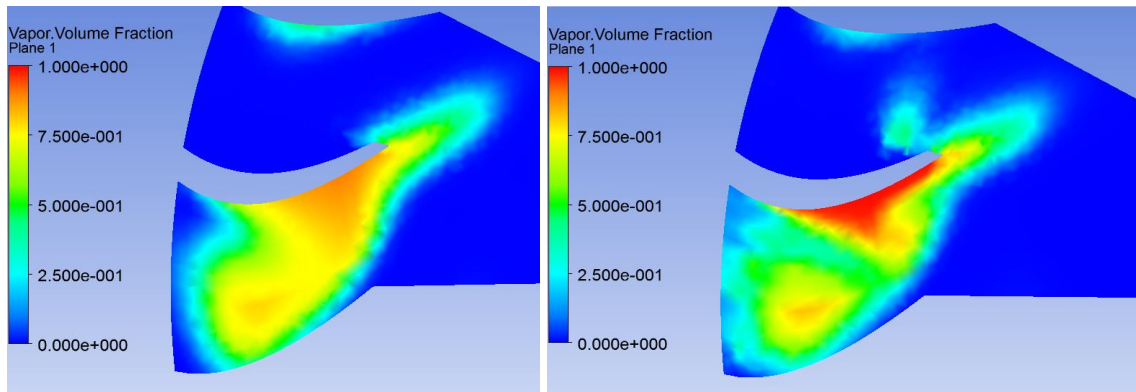


Figure 8.110: NVF(+)

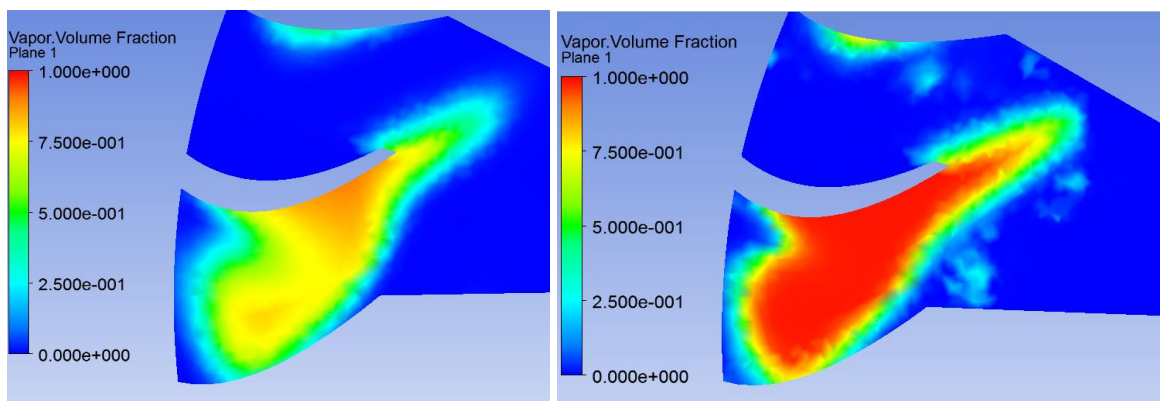


Figure 8.111: Mean diameter

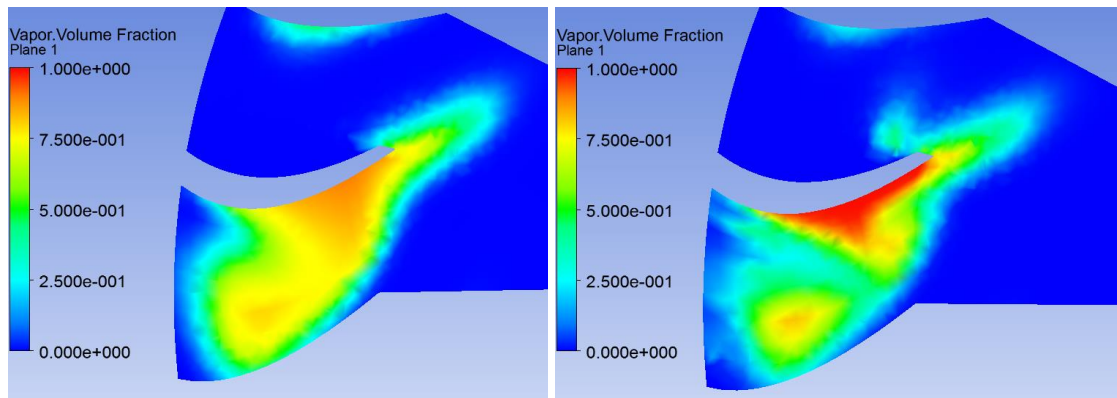


Figure 8.112: Fevaporation

The maximum amount of vapour increases in all the cases. However, the greatest impact occurs for the change of the value of the Mean diameter.

In the last simulation, the Nuclei Volume Fraction has been set to  $5 \cdot 10^{-6}$  in order to decrease the amount of vapour as it can be seen in the next figures. The impact on the vapour

volume fraction and its thickness is very strong since it almost disappears. However, the position and the shape do not change practically.

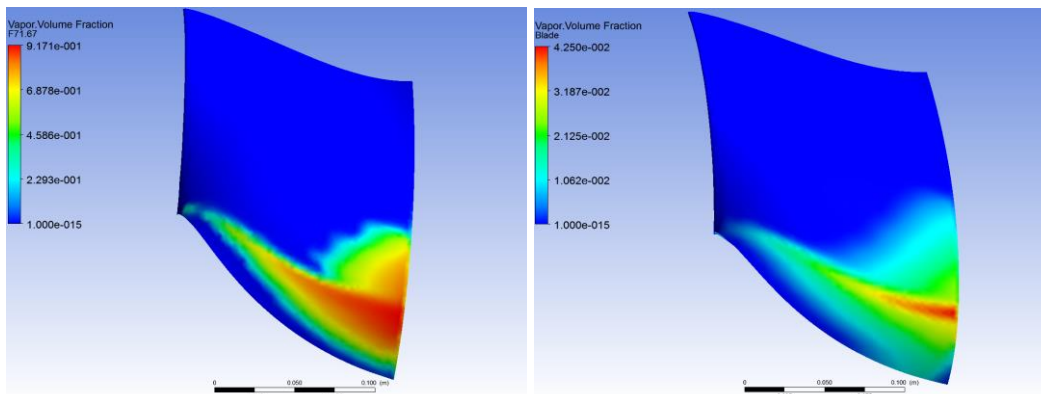


Figure 8.113: NVF(-)

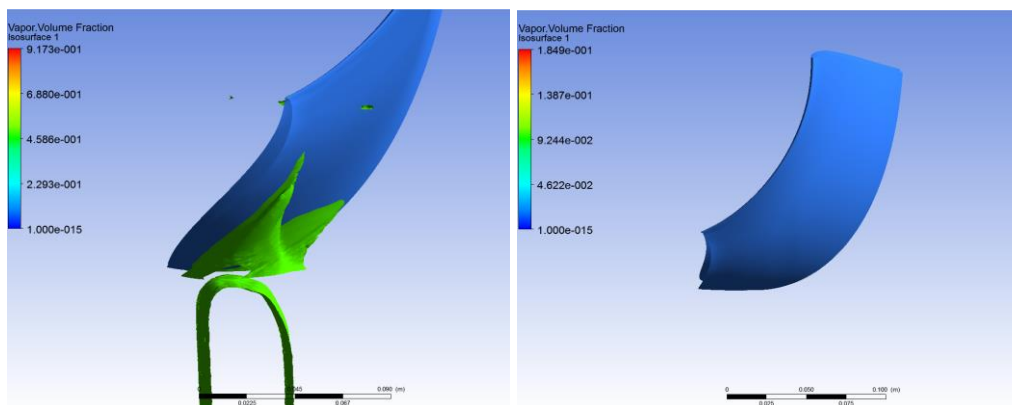


Figure 8.114: NVF(-)

Clearly, to set Nuclei Volume Fraction to  $5 \cdot 10^{-6}$  presents the highest impact on the amount of vapour. It can be explained because with the empirical parameters set to their default value the maximum amount of vapour is practically reached, however setting the NVF to  $5 \cdot 10^{-6}$  has a higher margin to decrease it.

The torque remains practically constant if the change of parameters promotes cavitation, because the blade area at vapour does not increase enough to change it. However, if the parameters are changed to decrease the amount of vapour, their effect on the torque is more significant. In the next table the value of the torque and its variation is indicated for each case.

Empirical Parameter	Torque (Nm)	% variation
Default	32,73	0
$F_{\text{condensation}} = 0,00001$	32,99	+0,8
$F_{\text{evaporation}} = 50000$	32,71	-0,06
Nuclei Volume Fraction = 0,5	32,67	-0,19
Mean Diameter = $2 \cdot 10^{-8}$ m	32,25	-1,46
Nuclei Volume Fraction = $5 \cdot 10^{-6}$	31,69	-3,16

Table 8.5

The main effect is to decrease the torque because the amount of vapour increases. However, the  $F_{\text{condensation}}$  has a reverse effect which provokes a torque increase.

In the next pictures, the pressure coefficient plotted on the blade for the simulation with the default values (right) is compared with the two most critical changes, Mean Diameter to  $2 \cdot 10^{-8}$  and Nuclei Volume Fraction to 0,5. It can be seen that the pressure coefficient practically does not change.

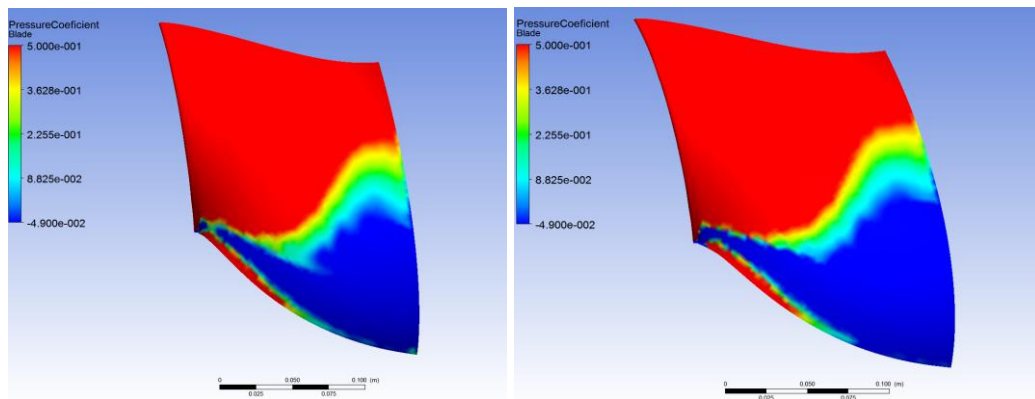


Figure 8.115: Mean diameter

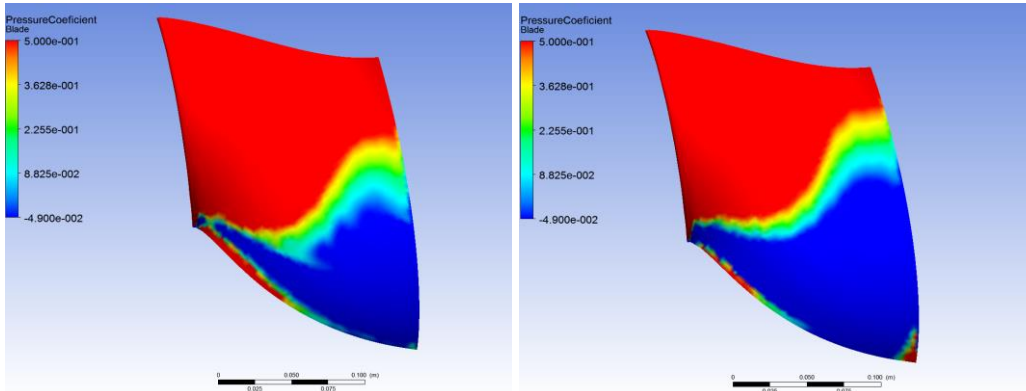


Figure 8.116: NVF(+)

It can be concluded that changing the empirical parameters only appears to change the vapour in the areas where the pressure is less than the vapour pressure, but the pressure distribution cannot be practically changed. For this reason, the impact on the results obtained setting Nuclei Volume Fraction to decrease the vapour, is higher since the study has been made for a low sigma condition where the maximum amount of vapour is already obtained using the default values. On the contrary, the margin to decrease the amount of vapour is much higher.

Using these extreme parameters the solution fluctuates a lot and more especially in the simulations with vapour increase.

In summary, it can be concluded that the effect of the empirical parameters can be significant, mainly concerning the amount of vapour and consequently the torque. For this reason, to test the model and to set the empirical parameters, a simple experiment on the laboratory is needed. Then with the model and the parameters tested, more complex simulations could be simulated with more precision.

## 9. Economic analysis

With regard to the budget, the next table details the employee expenditures, the cost per hour and the final cost of the project.

	Hours (h)	Cost per hour (€/h)	Total Cost (€)
Laptop	-	-	900
Printer	-	-	10
Phone and internet (6 month)	-	-	200
Consumption of light (6 month)	-	-	100
Office material	-	-	100
Educational license of Ansys (1 year)	-	-	2000
Educational license of SolidWorks (1 year)	-	-	2000
License of Microsoft office (1 year)	-	-	250
Hours of intern	455	12	5460
Hours of engineer	30	30	900
Total without VAT		11920 €	
Total with VAT (21%)		14423,2 €	

Table 9.6: Project budget

## 10. Environmental impact

The environment impact of this thesis is almost nothing since it has consisted solely in realizing simulations with a computer. As secondary function, it has also been used to look for the needed information and to be in touch with Xavier Escaler. Others devices used to make the thesis, which have energy consumption, are the calculator and the phone. However, the computer has been the device with highest energy consumption because the simulations have last for a long time even about eight hours.

On the other hand, paper, electricity due to the illumination, heating and ventilation, ink-jet printer and writing tools have also been used.

In the next table, the information about the energy consumption and its carbon dioxide production is shown:

	Power (KW)	Hours (h)	Energy (KWh)	CO <sub>2</sub> (Kg) [0.364 kg CO <sub>2</sub> /KWh]
Laptop	0,05	436	21,8	7,93
Phone	0,005	5	0,025	0,091
Illumination	0,5	485	242,5	88,27
Heating	1,5	50	75	27,3
Ventilation	0,04	242	9,68	3,52
Total	2,095	1218	349	127,11

*Table 10.7: Environmental study*

Finally, if this project were made by a company or a research institution, the material and the energy used to make the experimental prototype would have to be considered.

## 11. Work plan

In this section, the planning of the work is disaggregated with the main tasks like it can be seen in the next table.

Activity	Start date	Duration	Completion date
Documentation about static computational domain [1]	13/02/2017	7	20/02/2017
Static computation Domain [2]	20/02/2017	21	13/03/2017
Documentation about CFX [3]	27/02/2017	14	13/03/2017
Documentation about Turbulence Problem [4]	20/02/2017	21	13/03/2017
Documentation about RANS models [5]	27/02/2017	14	13/03/2017
Static simulations [6]	13/03/2017	7	20/03/2017
Documentation about Stage (CFX) ] [7]	13/03/2017	10	23/03/2017
Documentation about Stage computational domain [8]	13/03/2017	5	18/03/2017
Stage computational domain [9]	20/03/2017	3	23/03/2017
Stage simulations [10]	23/03/2017	14	06/04/2017
Documentation about cavitation [11]	03/04/2017	15	18/04/2017
Documentation about cavitation's model of CFX [12]	03/04/2017	3	06/04/2017
Sigma coefficient simulations [13]	06/04/2017	39	15/05/2017
Documentation about Fluid dynamics basic concepts [14]	18/04/2017	10	28/04/2017
Documentation about hydroplants and hydraulic turbines [15]	18/04/2017	7	25/04/2017
Documentation about Rayleigh-Plesset equation and ZGB model [16]	08/05/2017	7	15/05/2017
Report writing [17]	15/05/2017	32	16/06/2017
Study of sensitive of the ZGB model's empirics parameters [18]	15/05/2017	15	30/05/2017

Table 11.8: Tasks

In the next Gantt graph, the blue bars indicate the documentation tasks, which can be realized in parallel, however the red bars indicate the tasks which could not be overlapped between them and the green bar indicate the time dedicated to writing the report.

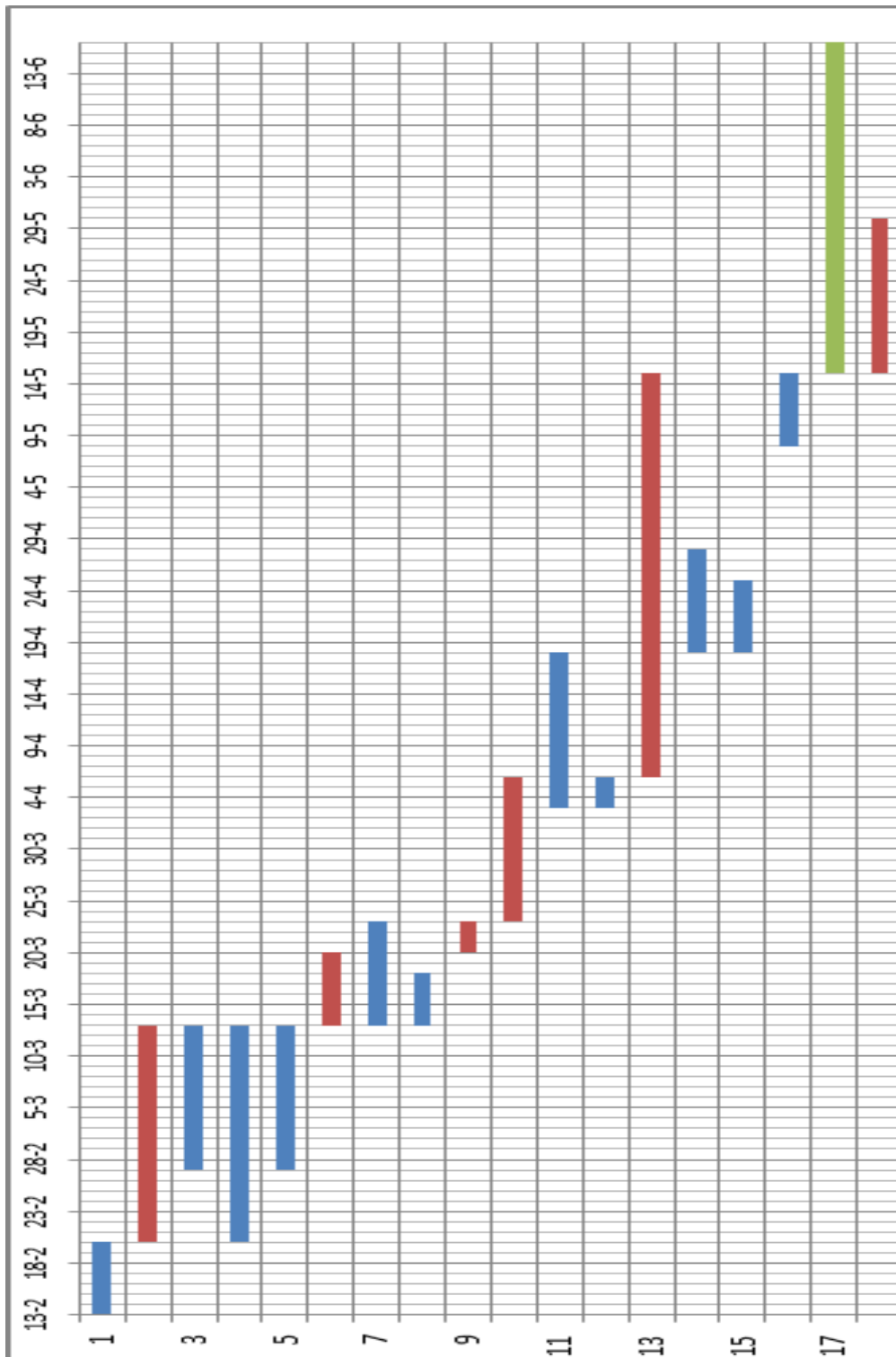


Figure 11.117: Work plan

## Conclusions

From this thesis work about the numerical simulation of the GAMM Francis turbine runner operation under cavitation conditions at BEP, the next conclusions have been obtained.

Firstly, a static model of the runner has been simulated. It has been concluded that the obtained results were too far from the reference ones due to obvious inaccuracies when setting the relative velocity at the inlet boundary. The calculated torque was lower than the one obtained from experimental measurements.

Consequently, it has been confirmed that it is a must to define a more complex model, called Stage steady-state, that considers a fluid domain rotating relative to a couple of static inlet and outlet domains. In this case, the simulated torque is very close to the experimental one.

To apply the Stage model, two interfaces separating the rotating and the static domains with different shapes at the outlet of the runner have been checked. It has been concluded that the best interface must be adjusted to the blade shape so that the fluid that leaves the blades enters a non-rotating region in the centre of the runner. In this case the convergence is not so fast but the results are more realistic.

From the simulations without cavitation, it has been observed that the highest forces on the blades are located around the outermost areas from the axis. This condition maximizes the torque.

Under cavitation conditions, two different types of cavities are observed. One small cavity is located at the leading edge which is more influenced by the fluid angle of attack than the Thoma number. The second type of cavitation appears downstream of the leading edge and increases its size significantly with the Thoma number as the typical travelling bubbles.

The incipient sigma value has been found around 0,99, and the critical sigma when the torque starts to drop due to the amount of vapour has been found around 0,35. However, the 3% drop of the torque due to developed cavitation has not been found due to the model limitations and uncertainties.

The empirical parameters of the cavitation model practically have no effect on the pressure distribution on the blade. However, they can sway on the amount of vapour appeared in the areas where the pressure is the vapour pressure and they can hinder the convergence of the results if extremes values are used.

In summary, the model limitations are due to the inlet and outlet boundary conditions. The

velocity field at the inlet boundary has been extrapolated from the available information at the runner inlet because the model considered does not include the guide vanes. The proximity of the outlet boundary to the runner does not permit to simulate the draft tube effects and the outlet pressure cannot be set far enough of the runner outlet to get enough pressure drop at the blades leading edges. To conclude the draft tube and the guide vanes are very important to simulate the cavitation phenomena.

For a future work, a transient simulation using a LES model to solve the turbulence problem is the best option to obtain highly realistic results. However, to solve this model requires a high computation capacity and long time, increasing the cost of the study. Moreover, if the guide vanes are not simulated, the cost of the project grows faster than the additional characteristics captured for the model making this option useless. For this reason, the Stage steady-state model is a good choice which has a less cost than the transient model and gives results that are good enough.

## Acknowledgement

Firstly, the author would like to acknowledge all his family for their unconditional support throughout the industrial's career, being there for him and encouraging him to go ahead in the most difficult times.

Secondly, but not least, the author would like to thanks Professor Xavier Escaler for to let him to work together for a one year highlighting their interest, availability, so important advices in order to complete the thesis and his endless patience during all the stages of the project. Moreover, Xavier Escaler has given to the author another view of the engineering approaching him to the research world and without a doubt making that this year has been the most interesting of the career. Finally, the author would also like to highlight that Xavier Escaler is an outstanding professional and overcoat an extraordinary person.

Finally, the author would like to thank their closest friends for easing this career and always give him their support.

## References

- [1] Notes of *Renewable Energy* course, Barcelona: ETSEIB-UPC 2015.
- [2] Notes of *Tecnologia Energètica* course, Barcelo: ETSEIB-UPC 2016.
- [3] Notes of *Màquines Hidrauliques* course, Barcelona: ETSEIB-UPC 2016.
- [4] Notes of *Mecànica de Fluids* course, Barcelona: ETSEIB-UPC 2014.
- [5] Santiago Laín Beatove, Manuel Julio García Ruiz, François Avellan, Brian Quintero Arboleda, Santiago Orrego Bustamante, *Simulación numérica de turbinas Francis*, Medellín: Fondo Editorial Universidad EAFIT, 2011.
- [6] François Avellan, *Introduction to cavitation in hydraulic machinery*, Scientific Bulletin of the Politehnica of Timisoara Transactions on Mechanics, 2004.
- [7] Ayancik, Fatma, Celebioglu, Kutay and Aradag, Selin, *Parametrical and theoretical design of a Francis turbine runner with the help of computational fluid dynamics*, 10<sup>th</sup> International Conference on Heat Transfer, Fluid Mechanics and Thermodynamics, Orlando, 14-16 July 2014.
- [8] Diego Córdoba, *Las ecuaciones de Navier-Stokes I*, Instituto de Ciencias Matemáticas.
- [9] Hakan Nilsson, Lars Davidson, *A validation of parallel multiblock CFD against the GAMM Francis water turbine runner at best efficiency and off-design operating conditions*, Goteborg: Department of Thermo and Fluid Dynamics-Chalmers University of Technology.
- [10] Romeo Susan-Resiga, Sebastian Muntean, Ioan Anton, Sandor Bernad, *Numerical investigation of 3D cavitating flow in Francis turbines*, 12<sup>th</sup> International Conference on Fluid Flow Technologies, Budapest, 3-6 September 2003.
- [11] Romeo Susan-Resiga, Sebastian Muntean, Ioan Anto, *Numerical analysis of cavitation inception in Francis turbine*, Proceedings of Hydraulic Machinery and Systems 21<sup>st</sup>, Lausanne, 9-12 September 2002.
- [12] B. Lewis, A. Wouden, J. Cimbala, E. Paterson, *OpenFOAM Validation of the GAMM Francis Runner using SimpleSRFFOAM*, 6<sup>th</sup> OpenFOAM Workshop, The Pennsylvania State University, 13-16 June 2011.

- [13] Sebastian Muntean, Sandor Bernerd, Romeo F. Susan-Resiga, Ioan Anton, *Analysis of the GAMM Francis turbine distributor 3D flow for the whole operating range and optimization of the guide vane axis location*, Scientific Bulletin of the Politehnica University of Timisoara Transactions on Mechanics.
- [14] H. Nilsson and L. Davidson, *Validations of CFD against detailed velocity and pressure measurements in water turbine runner flow*, Int. J. Numer. Meth. Fluids, 41, 200.
- [15] B. J. Lewis, *Improving Unsteady Hydroturbine Performance During Off-design Operation by injecting Water from the Trailing Edge of the Wicket Gates* (Doctoral Dissertation), The Pennsylvania State University, 2014.
- [16] [<https://www.learncax.com/knowledge-base/blog/by-category/cfd/basics-of-y-plus-boundary-layer-and-wall-function-in-turbulent-flows>]\*.\*[URL, date of consult].
- [17] [[https://www.cfd-online.com/Wiki/RANS-based\\_turbulence\\_models](https://www.cfd-online.com/Wiki/RANS-based_turbulence_models)]\*.\*[URL, date of consult].
- [18] G. Kuiper, *Cavitation in Ship Propulsion*, January 15, 2010, Nuclei11.
- [19] [<http://iamechatronics.com/notes/general-engineering/397-fluid-mechanics-law-of-continuity>]\*.\*[URL, date of consult].
- [20] [[https://www.sharcnet.ca/Software/Ansys/16.2.3/en-us/help/cfx\\_thry/cfxMultInteCavi.html#i1307195](https://www.sharcnet.ca/Software/Ansys/16.2.3/en-us/help/cfx_thry/cfxMultInteCavi.html#i1307195)]\*.\*[URL, date of consult].